Journal Pre-proof

Metallization of solar cells, exciton channel of plasmon photovoltaic effect in perovskite cells

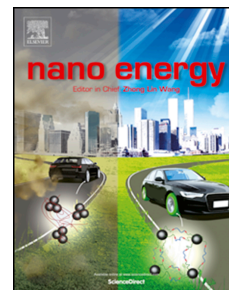M. Laska, Z. Krzemińska, K. Kluczyk-Korch, D. Schaadt, E. Popko, W.A. Jacak, J.E. Jacak

Please cite this article as: M. Laska, Z. Krzemińska, K. Kluczyk-Korch, D. Schaadt, E. Popko, W.A. Jacak, J.E. Jacak, Metallization of solar cells, exciton channel of plasmon photovoltaic effect in perovskite cells, *Nano Energy* (2020), doi: https://doi.org/10.1016/j.nanoen.2020.104751.

This is a PDF file of an article that has undergone enhancements after acceptance, such as the addition of a cover page and metadata, and formatting for readability, but it is not yet the definitive version of record. This version will undergo additional copyediting, typesetting and review before it is published in its final form, but we are providing this version to give early visibility of the article. Please note that, during the production process, errors may be discovered which could affect the content, and all legal disclaimers that apply to the journal pertain.
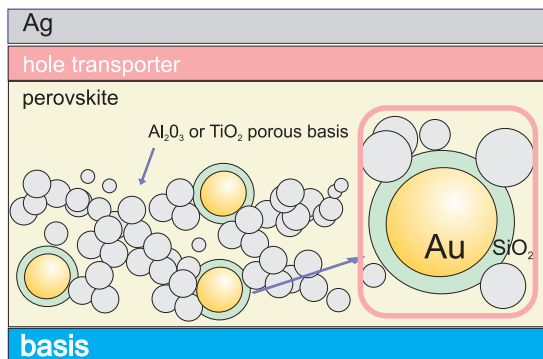
Graphical Abstract

Metallization of solar cells, exciton channel of plasmon photovoltaic effect in perovskite cells

M. Laska,Z. Krzemińska,K. Kluczyk-Korch,D. Schaadt,E. Popko,W. A. Jacak,J. E. Jacak

Highlights

Metallization of solar cells, exciton channel of plasmon photovoltaic effect in perovskite cells

M. Laska,Z. Krzemińska,K. Kluczyk-Korch,D. Schaadt,E. Popko,W. A. Jacak,J. E. Jacak

- microscopic theory of plasmon-mediated photo-absorption in $p - n$ junction-type cells is formulated

- microscopic theory of plasmon-mediated photo-absorption in exciton-type cells is formulated

- mechanism of reduction of exciton binding energy by coupling to plasmons is explained

- new mechanism of plasmon photovoltaic effect in perovskite cells is identified

- comparison to experiment with metalized hybrid perovskite solar cells of various type is presented

Metallization of solar cells, exciton channel of plasmon photovoltaic effect in perovskite cells

M. Laska[a], Z. Krzemińska[a], K. Kluczyk-Korch[b], D. Schaadt[c], E. Popko[a], W. A. Jacak[a] and J. E. Jacak[a,*]

[a]Department of Quantum Technology, Wrocław University of Science and Technology, Wyb. Wyspiańskiego 27, 50-370 Wrcław, Poland
[b]Department of Electronics Engineering, University of Rome Tor Vergata, Via del Politecnico 1, 00133 Rome, Italy
[c]Institute of Energy Research and Physical Technologies, Clausthal University of Technology, Germany

ARTICLE INFO

ABSTRACT

Metallic nanoparticles are used to improve solar cell efficiency due to plasmon mediated photovoltaic effect. We present various channels of this phenomenon in semiconductor solar cells with $p - n$ junction and in chemical-type cells with exciton photovoltaic mechanism. Besides of previously known by plasmon strengthening of sun light absorption in metalized solar cells we have described the influence of plasmonic nanoparticles onto internal electricity of cells. The latter case we analyze on the example of hybridized perovskite solar cells regarded as most promising cells of III-rd generation. The explanation of recent experimental achievements with the metallization of perovskite cells is presented in comparison to the metallization of conventional Si-based cells.

1. Introduction

Metallization of solar cells is a simple and cheap method to increase the efficiency of solar cells. By application of dilute surface coverings of cells with Au, Ag or Cu nanoparticles of size, $a \in (5, 50)$ nm (a is an averaged radius of nanoparticles), with surface concentration, $\sim 10^{8-10}$ /cm^2, a significant increase of the efficiency of solar batteries has been achieved, cf. e.g., Refs [1, 2, 3, 4, 5, 6, 7, 8, 9, 10] .

It is astonishing that relatively low dense coverings of metallic nanoparticles deposited on the photo-active surface of substrate semiconductor act as the very effective channels for solar energy transfer resulting in large increase of the photo-effect and in significant enhancement of the overall solar cell efficiency. In Table 1 we list several examples of relevant experiments with metallization of semiconductor cells related with Si photo-material with conventional $p - n$ junction configuration. Similar behavior exhibit also other semiconductor photo-diode configuration cells, like GaAs or CIGS thin films cells metalized with Au or Ag [11, 12].

The reason of the strengthening of the photo efficiency by metallic nanoparticles is related with a strong resonance of surface plasmons in metallic nanoparticles, which for Au, Ag or Cu conveniently overlaps with the visible sun-light spectrum and causes very effective absorption of incident sun-light photons in such metallic nanoparticles due to the symmetry of the absorption and emission in quantum transitions [13]. Due to coupling of oscillating dipoles of surface plasmons in metallic components to band electrons in the substrate semiconductor, the captured sun-light energy is instantly transferred to semiconductor and used for the excitation of electrons from the valence to the conduction band, strengthening overall light absorption. This is, however, only one channel of the plasmon photo-effect. The another one has been recently demonstrated in hybridized perovskite cells [14, 15, 16], where the large increase of the final efficiency of a cell has been occurred but not due to an enhancement of the light absorption solely. This second channel of the plasmon effect is related with the influence of metallic components onto internal electricity of a cell. Remarkably, the efficiency increase via this second channel has been observed in the chemical-type hybridized perovskite cells, i.e., in devices which belong to by exciton operating solar cells without $p - n$ junction.

In conventional semiconductor cells with the $p - n$ junction, the separation of carries ignited by the photon income or by coupling to plasmons, takes place due relatively large voltage of the junction (in Si ca. 0.7 V). Both sign carries, electron and holes separated by the voltage in $p - n$ junction, are next grasped by opposite electrodes. Active is only the $p - n$ junction region and excitons ignited in semiconductor regions distant from the junction weakly contribute to the

---

*Corresponding author, e-mail: janusz.jacak@pwr.edu.pl
ORCID(s): 0000-0003-0981-1566 (K. Kluczyk-Korch); 0000-0003-2645-7909 (W.A. Jacak); 0000-0002-6946-2495 (J.E. Jacak)

photo-current. Such excitons must diffuse to the junction region to be dissociated there which, however, takes a time increasing the probability of recombination of excitons. In $p - n$ type solar cells the strengthening of the absorption is of major importance. The other situation is in exciton-type chemical, plastic or hybrid solar cells. In these cells, called also as of III-rd generation cells, excitons are created in photo active centers like dye particles, quantum dots, in polymer or in ordinary semiconductor, and then these localized or moving excitons dissociate at the interface with electron (or hole) absorber due the difference of local band edges close to the minus (plus) electrode. In dye cells the role of the dissociation factor plays large gap semiconductor TiO_2 with highly developed surface in its porous phase, where electrons are captured from adjacent excitation centers. In all such solar cells, important is to improve the time rate of exciton dissociation. The reduction of the binding energy of excitons is convenient to increase the efficiency of their dissociation, which eventually increases the photo-current. Here is the place for the second channel of the plasmon photovoltaic effect.

In the present paper we describe both channels of the plasmon effect within the microscopic quantum approach. We indicate those factors which are important for the channels related to different solar cell operation types. For the quantitative assessments of the efficiency growth due to the discussed both channels we select two types of solar cells optimally attributed to both effects. The resulted theoretical estimations we compare with the experimental data for both selected cell types.

A special attention we will pay to metalized perovskite solar cells [14, 15, 16]. Perovskite solar cells born a great interest recently because their efficiency has been lifted to the level similar as of the best Si cells but by very low cost and simple conventional chemical technology of production including screen printing or ink-jet printing. Such technology of layer deposition makes the distribution of metallic components inside cell layers especially convenient and easy. The hybrid chemical perovskite cells operate according another fashion than the conventional semiconductor cells. They do not employ a $p - n$ junction but instead utilize the perovskite semiconductor layer in the double role of a dye and re-dox electrolyte upon the scheme of chemical dye cell. Incident photons excite excitons in the perovskite layer, which dissociate next at a porous interface with semiconductor of large gap (typically for such basis it is used TiO_2 or Al_2O_3) placed on the bottom of the perovskite layer. Electrons are here decoupled from excitons and penetrate the basis material due to the convenient relative energy level of conduction band edges of both touching each other semiconductors at the interface perovskite-basis. Electron diffuse through the basis to the negative electrode whereas holes leaved in the perovskite travel opposite direction to the positive electrode. As was evidenced experimentally, an application of metal nanoparticles in perovskite cells may improve their efficiency by ca. 20-40%, i.e., very large and even larger than in conventional $p - n$ cells as shown in Table 1, despite quite different microscopic operation fashion without $p - n$ junction. In the present paper we explain the physical mechanism of the specific plasmon effect in perovskite cells.

Metal	Size [nm]	Shape	Concentration	Enhancement	p-n depth [nm]	Type	Ref.
Au	50	spherical	$6.6 \cdot 10^8$ [cm^{-2}]	18% (max[a]:80%)			
Au	80	spherical	$1.6 \cdot 10^8$ [cm^{-2}]	31% (max[a]:100%)	80	c-Si	[1]
Au	100	spherical	$0.77 \cdot 10^8$ [cm^{-2}]	38% (max[a]:60%)			
Au	100	spherical	$9.9 \cdot 10^8$[cm^{-2}]	2.8%	500	c-Si[b]	[4]
Au	100	spherical	$0.3 \cdot 10^8$ [cm^{-2}]	5.6%			
Au	100	spherical	$1.5 \cdot 10^8$ [cm^{-2}]	2.0%	> 500[c]		
Au	100	spherical	$3.2 \cdot 10^8$ [cm^{-2}]	3.3%		mc-Si[d]	[3]
Au	100	spherical	$3.5 \cdot 10^8$ [cm^{-2}]	3.3%	500	c-Si[e]	[2]
Au	20 : [2; 3]	island	$1.3 \cdot 10^{11}$ [cm^{-2}]	20% (max[a]:40%)		a-Si:H/c-Si[f]	[5]
Au	65	spherical	$10 \cdot 10^8$ [cm^{-2}]	18%	300	c-Si[f]	[6]
Ag	40	island	$124 \cdot 10^8$ [cm^{-2}]	127%	160	SOI[h]	
Ag	66	island	$67 \cdot 10^8$ [cm^{-2}]	283%	160	SOI[h]	[8]
Ag	108	island	$25 \cdot 10^8$ [cm^{-2}]	592%	160	SOI[h]	
Ag	12, 14, 16[i]	island	-	19%, 14%, 2%[p]	-	Si	[7]
Ag	[120; 140] : [45; 60]	island	$30 \cdot 10^8$[cm^{-2}]	354%	95	SOI[g]	[9]
Ag	12 and 16[i]	island	-	33% and 16%	1250	SOI[j]	[7]
Ag	25 : 91	spheroidal	38%[l]	17%		c-Si[k]	
Al	22 : 81	spheroidal	40%	21%	-	c-Si[k]	[17]
In	17 : 25	spheroidal	30%	23%	-	c-Si[k]	
Ag	~ 60	island	31%	0%	> 150[m]	c-Si	[18]
Al	190 : 70	cylindrical	19%[o]	49%		c-Si[n]	[19]

Table 1

For various setups and nanoparticles deposition parameters the different increase of the photo-effect efficiency has been observed experimentally as reported in the indicated references. Majority of the observed behavior cannot be explained by only local concentration of the e-m field near the curvature of nanoparticles accounted for by the conventional Comsol modeling and the consistence of the experimental data with the theoretical simulation needs inclusion of the plasmon damping contribution as described in the present paper. However, some exceptionally low efficiency increase (or even decrease) evidences the complicated competition of various factors beyond the model considered in the paper, being apparently sensitive to the position of the p-n junction active layer in the substrate or to the interference destructive effects or reflection from too dense coverings; [a]the maximal value of absorption enhancement per single wavelength, [b]commercially available n/p Si solar cell produced by Silicon Solar Inc., [c]emitter thickness is 500 nm, [d]anti-reflection coating from SiN of thickness 70 nm, [e]n-type Si wafer (001) of thickness 300 μm and donor concentration ca. 10^{15} cm^{-3}, [h]silicon-on-insulator (SOI), [f]heterojunction a-Si:H/c-Si (p-type,(100)); the thickness of a-Si:H layer is 18 nm, [g]Si wafer with transparent graphene electrode, [i]nanoparticle coverage was fabricated by annealing of silver film of a particular thickness (12, 14, 16 nm) in the temperature 200°C by 50 minutes, [j]silicon-on-insulator (SOI); top Si layer thickness 1250 nm, [k]solar cell covered by 20 nm layer of TiO$_2$ separating nanoparticles form silicon, [l]for dense coverings the percentage of metalized surface is shown, [m]emitter thickness is 150 nm, [n]solar cell covered by 40 nm layer of SiO$_2$ separating nanoparticles from silicon, [o]periodic, period 380 nm, [p]enhancement averaged over the solar spectrum AM1.5G.

2. Mechanism of plasmon photovoltaic effect

The coupling of surface plasmons to the electron band system in the nearby semiconductor depends on the metallic nanoparticle size, concentration and deposition type, spatial separation with respect to the semiconductor, material parameters of metal and semiconductor. The eventual efficiency of the plasmon mediation results from the trade-off of several competing factors. Smaller nanoparticles better concentrate the electric field of the incident e-m wave and strengthen coupling to electrons but simultaneously reduce the number of electrons oscillating in nanoparticles, which quenches the amplitude of plasmon dipole. Too dense particle distributions paradoxically reduce efficiency because of collective interference reflection of light by simple blackout of the photo-cell or by the creation of collective parasitic excitations in dense metallic arrays decoupling plasmons from band electrons in the substrate semiconductor. Moreover, the presence of metallic elements influences the quantum microscopic properties of the semiconductor substrate and of metallic nanoparticle themselves. They are different in comparison to the same but separated elements. Irradiation of plasmon from the metallic nanoparticle deposited on the semiconductor surface is different than the irradiation of plasmon in the nanoparticle in vacuum or in a dielectric surroundings. Similarly, the absorption of the semiconductor strongly changes due to the presence of metallic nanoparticles. These mutually dependent effects are strong and quantum in nature. They cannot be accounted for by the conventional plasmonic approach by solution of Maxwell-Fresnel equations with boundary condition adjusted to the geometry of the system. Such standard methods, like Mie theory [20] or the numerical solution of Maxwell equations (e.g., by finite element method, like by COMSOL) do not account for these effects as they utilize as prerequisites the dielectric functions of both materials measured in bulk and separated. The relative error in assessment of the plasmon effect efficiency by COMSOL is ca. 90% [21], which completely dismisses modeling of the plasmon photovoltaic effect utilizing conventional COMSOL packets or Mie approach. This evidences that the strengthening of the electric field near a curvature of the metallic component, which is correctly calculated by Mie method or by COMSOL, is far insufficient to explain plasmon photovoltaic effect (as illustrated in Appendix D).

To properly account for the coupling of the plasmon in metallic nanoparticle to the band electron system in nearby semiconductor one must utilize the Fermi golden rule (FGR) to calculate probability of electron interband transitions induced by the plasmon oscillations. In the present paper we shortly remind this method originally developed by us for conventional semiconductor solar cells (Si, CIGS or GaAs) [22, 10, 12] and accommodate it to hybrid chemical perovskite-type cells.

The interaction of plasmons with electrons in the semiconductor substrate describes the retarded electro-magnetic field of the oscillating dipole in the metallic sphere with radius a. Fourier components of the magnetic ($\mathbf{B}_\omega$) and electric ($\mathbf{E}_\omega$) fields produced at a distant point $\mathbf{R}$ by monochromatic plasmon dipole oscillation at the origin, $\mathbf{D} = \mathbf{D}_0 e^{-i\omega t}$, have the form [23, 24],

$$\mathbf{B}_\omega = \frac{ik}{\sqrt{\varepsilon}}[\mathbf{D}_0 \times \hat{\mathbf{n}}]\left(\frac{ik}{R} - \frac{1}{R^2}\right)e^{ikR} \tag{1}$$

and

$$\mathbf{E}_\omega = \frac{1}{\varepsilon}\left\{\mathbf{D}_0\left(\frac{k^2}{R} + \frac{ik}{R^2} - \frac{1}{R^3}\right) + \hat{\mathbf{n}}(\hat{\mathbf{n}} \cdot \mathbf{D}_0)\left(-\frac{k^2}{R} - \frac{3ik}{R^2} + \frac{3}{R^3}\right)\right\}e^{ikR}, \tag{2}$$

where we use the following notation for the retarded argument: $i\omega\left(t - \frac{R}{c}\right) = i\omega t - ikR$ and $\hat{\mathbf{n}} = \frac{\mathbf{R}}{R}$. The contributions with denominators of R^3, R^2, and R are referred to as the near-, medium- and far-field zones of the dipole radiation, respectively. For interactions with the adjacent layer of the semiconductor, the near-field zone is of the most significance. One can therefore neglect the terms containing $\frac{1}{R}$ and $\frac{1}{R^2}$. Under the further assumption that $e^{ikR} = 1$ for the near field, one can obtain, $\mathbf{B}_\omega = 0$ and $\mathbf{E}_\omega = \frac{1}{\varepsilon R^3}\left[3\hat{\mathbf{n}}\left(\hat{\mathbf{n}} \cdot \mathbf{D}_0\right) - \mathbf{D}_0\right]$, which corresponds to the dipole electric field (ε is the dielectric permittivity of the surrounding medium). The magnetic field disappears in the near-field zone. In this zone photons are not created yet on so small distance much lower than the resonant wavelength (being of order of 0.5 μm). Hence, the related potential for the near-field interaction of the dipole Mie-type surface plasmons with the band electrons can be written as follows [12],

$$w = e\psi(\mathbf{R}, t) = \frac{e}{\varepsilon R^2}\hat{\mathbf{n}} \cdot \mathbf{D}_0 sin(\omega t + \alpha) = w^+ e^{i\omega t} + w^- e^{-i\omega t},$$
$$w^+ = (w^-)^* = \frac{e}{\varepsilon R^2}\frac{e^{i\alpha}}{2i}\hat{\mathbf{n}} \cdot \mathbf{D}_0. \tag{3}$$

The terms w^+ and w^- correspond to emission and absorption, respectively ($\hat{\mathbf{n}} = \frac{\mathbf{R}}{R}$, and $\mathbf{D}_0$ is the plasmon dipole amplitude). We choose to consider the emission of energy from the plasmon oscillations and the transfer of this energy to the electron system in the semiconductor substrate.

The semiconductor band system will be modeled here in the simplest form, in the single-band parabolic effective mass approximation. According to the Fermi golden rule, the inter-band transition probability is given by the expression [13],

$$w(\mathbf{k}_1, \mathbf{k}_2) = \frac{2\pi}{\hbar} \left| < \mathbf{k}_1 | w^+ | \mathbf{k}_2 > \right|^2 \delta(E_p(\mathbf{k}_1) - E_n(\mathbf{k}_2) + \hbar\omega), \tag{4}$$

where the Bloch states in the conduction and valence bands are assumed to be plane waves (for the sake of simplicity):

$$\Psi_{\mathbf{k}_1} = \frac{1}{(2\pi)^{3/2}} e^{i\mathbf{k}_1 \cdot \mathbf{R} - iE_p(\mathbf{k}_1)t/\hbar}, \Psi_{\mathbf{k}_2} = \frac{1}{(2\pi)^{3/2}} e^{i\mathbf{k}_2 \cdot \mathbf{R} - iE_n(\mathbf{k}_2)t/\hbar},$$
$$E_p(\mathbf{k}_1) = -\frac{\hbar^2 \mathbf{k}_1^2}{2m_p^*} - E_g, E_n(\mathbf{k}_2) = \frac{\hbar^2 \mathbf{k}_2^2}{2m_n^*}, \tag{5}$$

where the indices n and p refer to electrons from the conduction and valence bands, respectively, and E_g is the forbidden gap.

Here, let us make a technical comment. The electron wave functions as given above are assumed to be normalized to the Dirac delta, which corresponds to infinite movement and a continuous energy spectrum. The square of the wave function modulus does not, in this case, support the probability interpretation, which must be normalized to unity. To restore the proper normalization, the expression, $w(\mathbf{k}_1, \mathbf{k}_2) = \frac{2\pi}{\hbar} \left| < \mathbf{k}_1 | w^+ | \mathbf{k}_2 > \right|^2 \delta(E_p(\mathbf{k}_1) - E_n(\mathbf{k}_2) + \hbar\omega)$ must be divided by the Dirac delta square which can be expressed by the factor, $\left(\frac{V}{(2\pi)^3}\right)^2$, taking into account that,

$$\frac{1}{(2\pi)^3} \int d^3 r e^{i\mathbf{k}\cdot\mathbf{r}} = \delta(\mathbf{k}) \simeq \text{ (for } \mathbf{k} = 0) \frac{V}{(2\pi)^3} (V \to \infty). \tag{6}$$

The same factor occurs, however, due to the density of states, when one integrates over all initial and final states $\mathbf{k}_1, \mathbf{k}_2$, which results in the factor $\left(\frac{2V}{(2\pi)^3}\right)^2$ (the factor of 2 arises because of spin degeneracy). Thus, both renormalization factors mutually cancel. Taking into account the above described renormalization, we must find the matrix element,

$$< \mathbf{k}_1 | w^+ | \mathbf{k}_2 > = \frac{1}{(2\pi)^3} \int d^3 R \frac{e}{\varepsilon 2i} e^{i\alpha} \hat{\mathbf{n}} \cdot \mathbf{D}_0 \frac{1}{R^2} e^{-i(\mathbf{k}_1 - \mathbf{k}_2)\cdot\mathbf{R}}. \tag{7}$$

All integrals can be computed here analytically. After some algebra (cf. Appendix A), one arrives at the expression,

$$< \mathbf{k}_1 | w^+ | \mathbf{k}_2 > = \frac{-1}{(2\pi)^3} \frac{ee^{i\alpha}}{\varepsilon} D_0 cos\Theta(2\pi) \int_a^\infty dR \frac{1}{q} \frac{d}{dR} \frac{sinqR}{qR}$$
$$= \frac{1}{(2\pi)^2} \frac{ee^{i\alpha}}{\varepsilon} \frac{\mathbf{D}_0 \cdot \mathbf{q}}{q^2} \frac{sinqa}{qa} \to a \to 0 \frac{1}{(2\pi)^2} \frac{ee^{i\alpha}}{\varepsilon} \frac{\mathbf{D}_0 \cdot \mathbf{q}}{q^2}. \tag{8}$$

To estimate the absorption probability (per time unit according to the FGR scheme [13]), the summation over all initial and final states in both bands must be performed. Thus, we arrive at the formula for the transition probability,

$$\delta w = \int d^3 k_1 \int d^3 k_2 \left[f_1(1 - f_2) w(\mathbf{k}_1, \mathbf{k}_2) - f_2(1 - f_1) w(\mathbf{k}_2, \mathbf{k}_1) \right], \tag{9}$$

where f_1 and f_2 represent the temperature-dependent distribution functions (Fermi-Dirac distribution functions) for the initial and final states, respectively. Emission and absorption are included, but for room temperature, one can assume that $f_2 \simeq 0$ and $f_1 \simeq 1$, leading to,

$$\delta w = \int d^3 k_1 \int d^3 k_2 \cdot w(\mathbf{k}_1, \mathbf{k}_2). \tag{10}$$

In the above formula, we eliminated the state density factors through probability normalization, as mentioned above. After the integration we arrive at the expression (cf. Appendix A),

$$
\begin{aligned}
\delta w &= \frac{4}{3} \frac{\mu^2 (m_n^* + m_p^*) 2(\hbar\omega - E_g) e^2 D_0^2}{\sqrt{m_n^* m_p^*} 2\pi\hbar^5 \varepsilon^2} \int_0^1 dx \frac{sin^2(xa\xi)}{(xa\xi)^2} \sqrt{1 - x^2} \\
&= \frac{4}{3} \frac{\mu^2}{\sqrt{m_n^* m_p^*}} \frac{e^2 D_0^2}{2\pi\hbar^3 \varepsilon^2} \xi^2 \int_0^1 dx \frac{sin^2(xa\xi)}{(xa\xi)^2} \sqrt{1 - x^2}.
\end{aligned}
\tag{11}
$$

In limiting cases we ultimately obtain,

$$
\delta w = \begin{cases} \frac{4}{3} \frac{\mu \sqrt{m_n^* m_p^*}(\hbar\omega - E_g) e^2 D_0^2}{\hbar^5 \varepsilon^2}, & \text{for } a\xi \ll 1, \\ \frac{4}{3} \frac{\mu^{3/2} \sqrt{2} \sqrt{\hbar\omega - E_g} e^2 D_0^2}{a\hbar^4 \varepsilon^2}, & \text{for } a\xi \gg 1, \end{cases}
\tag{12}
$$

where the parameter $\xi = \frac{\sqrt{2(\hbar\omega - E_g)(m_n^* + m_p^*)}}{\hbar}$ allows for the definition of small nanoparticles $a\xi \ll 1$ and larger ones $a\xi \gg 1$. In the latter case in Eq. (12) we have applied the approximation,

$$
\int_0^1 dx \frac{sin^2(xa\xi)}{(xa\xi)^2} \sqrt{1 - x^2} \approx (\text{for } a\xi \gg 1) \frac{1}{a\xi} \int_0^\infty d(xa\xi) \frac{sin^2(xa\xi)}{(xa\xi)^2} = \frac{\pi}{2a\xi},
$$

whereas in the former case, $\int_0^1 dx \sqrt{1 - x^2} = \pi/4$.

The above formulae are distinct than the corresponding formula for the ordinary photo-effect. In the case of ordinary photo-effect, the perturbation is given by the vector potential in the kinematic momentum (for gauge of the vector potential $\mathbf{A}$, $div\mathbf{A} = 0$),

$$
\hat{H} = \frac{(-i\hbar\nabla - \frac{e}{c}\mathbf{A}(\mathbf{R}, t))^2}{2m^*} \simeq \frac{(-i\hbar\nabla)^2}{2m^*} + \frac{i\hbar e}{m^* c}\mathbf{A}(\mathbf{R}, t) \cdot \nabla.
\tag{13}
$$

For a monochromatic plane wave this perturbation has the form,

$$
\begin{aligned}
w_0(\mathbf{R}, t) &= \frac{ie\hbar}{cm^*} cos(\omega t - \mathbf{k} \cdot \mathbf{R} + \alpha)(\mathbf{A}_0 \cdot \nabla) \\
&= \frac{ie\hbar}{2cm^*} (e^{i(\omega t - \mathbf{k} \cdot \mathbf{R} + \alpha)} + e^{-i(\omega t - \mathbf{k} \cdot \mathbf{R} + \alpha)})(\mathbf{A}_0 \cdot \nabla).
\end{aligned}
\tag{14}
$$

Because in this case, both states of the band electrons and of the photon have the form of plane waves, the matrix element in the Fermi golden rule is proportional to the Dirac delta with respect to the momentum sum. This proportionality expresses momentum conservation in a translationally invariant system, which is the case for a photon interacting with a semiconductor,

$$
\begin{aligned}
< \mathbf{k}_1 | w_0(\mathbf{R}, t) | \mathbf{k}_2 > &= \frac{i\hbar e}{2cm^*(2\pi)^3} \int d^3 R e^{-i(\mathbf{k}_1 + \mathbf{k}) \cdot \mathbf{R}} (\mathbf{A}_0 \cdot \nabla) e^{i\mathbf{k}_2 \cdot \mathbf{R}} \\
&= -\frac{e\hbar}{2cm^*} \mathbf{A}_0 \cdot \mathbf{k}_2 \delta(\mathbf{k}_1 + \mathbf{k} - \mathbf{k}_2).
\end{aligned}
\tag{15}
$$

Because of the high value of the photon velocity c, the photon momentum $\mathbf{k}$ is negligibly small, and thus only vertical transitions, $\mathbf{k}_1 = \mathbf{k}_2$, are permitted in the ordinary photo-effect.

However, this is not the case for nanosphere plasmons interacting in the near-field regime with the semiconductor substrate. This system is not translationally invariant and excitations other than vertical are permitted, which results in the enhancement of the total transition probability.

For comparison with the ordinary photo-effect, let us recall the appropriate calculus based on the Fermi golden rule scheme for the ordinary photo-effect, for which,

$$
w_0(\mathbf{k}_1, \mathbf{k}_2) = \frac{\pi e^2 \hbar}{2c^2 m^{*2}} k_2^2 A_0^2 cos^2\Theta \delta^2(\mathbf{k}_1 - \mathbf{k}_2) \delta(E_p - E_n + \hbar\omega),
\tag{16}
$$

where Θ is the angle between $\mathbf{k}_2$ and $\mathbf{A}_0$. One can use the following approximation to eliminate the Dirac delta squared:

$$
\delta^2(\mathbf{k}_1 - \mathbf{k}_2) = \delta(0)\delta(\mathbf{k}_1 - \mathbf{k}_2) \simeq \frac{V}{(2\pi)^3}\delta(\mathbf{k}_1 - \mathbf{k}_2).
\tag{17}
$$

Similar to the previous discussion, the probability normalization must be performed. Thus, we obtain,

$$w_0(\mathbf{k}_1, \mathbf{k}_2) = \frac{\pi e^2 \hbar}{2c^2 m^{*2}} \frac{V}{(2\pi)^3} k_2^2 A_0^2 cos^2 \Theta \delta(\mathbf{k}_1 - \mathbf{k}_2) \delta(E_p - E_n + \hbar\omega). \tag{18}$$

The integration over all states in both electron bands results in,

$$\delta w_0 = \int d^3 k_1 \int d^3 k_2 \frac{\pi e^2 \hbar}{2c^2 m^{*2}} \frac{V}{(2\pi)^3} k_2^2 A_0^2 cos^2 \Theta \delta(\mathbf{k}_1 - \mathbf{k}_2) \delta(E_p - E_n + \hbar\omega), \tag{19}$$

or

$$\delta w_0 = \int d^3 k_2 \frac{\pi e^2 \hbar}{2c^2 m_p^{*2}} \frac{V}{(2\pi)^3} k_2^2 A_0^2 cos^2 \Theta \delta(E_p(\mathbf{k}_2) - E_n(\mathbf{k}_2) + \hbar\omega), \tag{20}$$

where the effective mass in the initial valence state is m_p^* (moreover, $A_0 = \frac{c}{\omega} E_0$). We thus obtain

$$\delta w_0 = \frac{1}{12} \frac{e^2 \hbar}{m_p^{*2}} \frac{V}{\pi} \frac{E_0^2}{\omega^2} \frac{2^{3/2} \mu^{5/2}}{\hbar^5} (\hbar\omega - E_g)^{3/2}. \tag{21}$$

This expression can be rewritten as,

$$\delta w_0 = \frac{4\sqrt{2}}{3} \frac{\mu^{5/2} e^2}{m_p^{*2} \omega \varepsilon \hbar^3} \left(\frac{\varepsilon E_0^2 V}{8\pi \hbar \omega} \right) (\hbar\omega - E_g)^{3/2}; \tag{22}$$

this expression should be multiplied by 4 (because of spin degeneracy, although for circular polarization of the photons this factor is only equal to 2 because of angular momentum selection rules). The factor $\left(\frac{\varepsilon E_0^2 V}{8\pi \hbar \omega} \right)$ extracted in the above formula is the number of photons $\hbar\omega$ in the volume V at the light intensity $\sim E_0^2$, the division by this factor gives the probability of the interband transition counted per single incident photon (the same renormalization per single photon can be done also for Eq. (11)).

3. Two channels for the plasmon photo-voltaic effect

3.1. Reducing of the binding energy of excitons excited by plasmons

Found above probabilities of the interband transitions induced by plasmons (12) and by photons (21) display a deep difference between these two effects. At the ordinary photo-effect induced by photons, Eq. (21), only vertical interband transitions are admitted. The reason of it is the form of perturbation of the electron band system by incident photons. Photons correspond to plane waves, $\mathbf{A}_0 e^{i(\mathbf{p}\cdot\mathbf{r} - \omega t)}$ (it is a vector potential of incident e-m wave) and the perturbation of the Hamiltonian has the form given by Eq. (14). The Fourier component shape of this perturbation causes the Dirac delta in Eq. (15), which expresses the momentum conservation (the momentum is $\hbar\mathbf{k}_i$). The momentum of photon $\hbar k = \hbar\omega/c$ is extremely small on the scale of the first Brillouin zone in the semiconductors (because of high value of c) and thus $\mathbf{k}_1$ is practically equal to $\mathbf{k}_2$, i.e., the transitions are vertical in the band structure. For the plasmon induced transitions we do not deal with such a restriction because the potential has the infinite Fourier decomposition and all nonvertical interband transitions are admitted. Thus excitons ignited by photos have always $\mathbf{q} = \mathbf{k}_1 - \mathbf{k}_2$ equal to zero, whereas if ignited by plasmons have nonzero $\mathbf{q}$, in general. Nonzero $\mathbf{q}$ causes the reduction of the exciton binding energy.

To illustrate it let us consider electron-hole (e-h) pair with the reduced mass $\mu = \frac{m_n^* m_p^*}{m_p^* + m_n^*}$, where m_n^* is the effective mass of electron in the conductivity band and m_p^* the hole mass in the valence band. When the relative momentum of the pair $\mathbf{k}_1 - \mathbf{k}_2 = \mathbf{q}$ is nonzero, where $\mathbf{k}_{1(2)}$ is the pseudomomentum of electron (hole), then this nonzero relative momentum tends to separate the e-h pair. Assuming that at $q = 0$ the binding energy of the exciton e-h is $E < 0$, then for $\frac{\hbar^2 q^2}{2\mu} > |E|$ the exciton will dissociate. The state E in the lowest energy in the well of mutual Coulomb attraction of electron and hole, $-\frac{e^2}{\varepsilon r}$ (or in SI units, $-\frac{e^2}{4\pi\varepsilon_0 \varepsilon r}$), for a particle with the reduced mass μ (r is the relative distance

between electron and hole—the size of the exciton, ε is the permittivity of the semiconductor). The averaged energy of the particle with mass μ in this well has the form (with kinetical energy assessed by the uncertainty principle),

$$E(r) = \frac{\hbar^2}{2\mu r^2} - \frac{e^2}{\varepsilon r}, \tag{23}$$

which has a minimum $E(r^*) = -\frac{e^4 \mu}{2\hbar^2 \varepsilon^2}$ at $r^* = \frac{\hbar^2 \varepsilon}{\mu e^2}$. This is a binding energy of the exciton $E = E(r^*)$, whereas r^* is the exciton size. If the pair has nonzero q (which is the same at any inertial system, note that for $P = |\mathbf{k}_1 + \mathbf{k}_2|$ always it exists an inertial system in which $P = 0$, but for q not) the minimal value of energy in the hyperbolic well of Coulomb attraction of e-h pair equals to $E(r^*) + \frac{\hbar^2 q^2}{2\mu}$. When $\frac{\hbar^2 q^2}{2\mu} = E(r^*)$, the e-h pair does not form a coupled state—the exciton dissociates. For smaller values of q the binding energy of exciton is still negative, $E(r^*) + \frac{\hbar^2 q^2}{2\mu}$, which defines also the new size of the exciton, $r^{**} = \frac{e^2}{-E(r^*)+\hbar^2 q^2/2\mu}$.

We see that excitons with nonzero q are weaker bound and easier dissociate. In solar cells, such weaker coupled photo-excited excitons stronger contribute to the photo-current.

To account it more precisely, let us estimate the averaged reduction of the binding energy of exciton. The binding energy of the exciton with $q = 0$ is assessed according the effective atom Bohr-like model, for which the binding energy is given by the formula,

$$E(n) = -\frac{\mu R_H}{m \varepsilon^2 n^2}, \tag{24}$$

where, $\mu = \frac{m_n^* m_p^*}{m_n^* + m_p^*}$ is the reduced mass of electron and hole, m is the mass of free electron, $R_H = 13.6$ eV is the Rydberg constant, ε is the permittivity of the semiconductor, n enumerates the ground ($n = 1$) and excited states of the exciton, the same as given by the lowest mean energy in hyperbolic well, $E(r^*)$.

The reduction of the binding energy for the exciton with relative momentum q is given by, $\Delta E(q) = \frac{\hbar^2 q^2}{2\mu}$. This value must be averaged over the probability transition between $\mathbf{k}_1$ and $\mathbf{k}_2$ states acc. to the formula (8). After summation over all initial and final states we arrive with the formula,

$$\Delta E = \frac{\int d^3 k_1 \int d^3 k_2 \frac{\hbar^2 q^2}{2\mu} w(\mathbf{k}_1, \mathbf{k}_2)}{\int d^3 k_1 \int d^3 k_2 w(\mathbf{k}_1, \mathbf{k}_2)}. \tag{25}$$

One can perform integrations analytically (as demonstrated in Appendix A), which leads to the expression,

$$\Delta E(a) = \frac{\frac{\hbar^2}{2\mu} \int_0^1 dx \frac{\sin^2(xb\xi)}{b^2} \sqrt{1-x^2}}{\int_0^1 dx \frac{\sin^2(xb\xi)}{(xb\xi)^2} \sqrt{1-x^2}}, \tag{26}$$

where $b = a + d$ (d is the insulator shell thickness), μ is the reduced mass of the e-h pair and $\xi = \frac{\sqrt{2(\hbar\omega - E_g)(m_n^* + m_p^*)}}{\hbar}$. This function is plotted in Fig. 1.
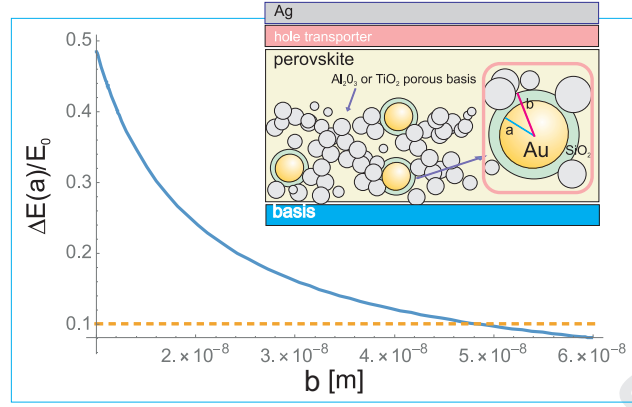
Figure 1: Averaged reduction of the exciton binding energy induced by the interaction with surface dipole plasmon in metallic nanoparticle (with radius a) embedded in the perovskite layer. The binding energy shift is renormalized by the energy on the border of the Brillouin zone, $E_0 = \frac{\hbar^2 p_0^2}{2\mu}$, where $p_0 = \pi/l$ and $l \simeq 5$ nm is the averaged linear size of the elementary cell of perovskite ($E_0 \sim 200$ meV for $\mu \sim 0.35m$, cf. [15]).

One can estimate this contribution for perovskite $CH_3NH_3PbI_{3-\alpha}Cl_\alpha$ cells with the crystal lattice cell axes, $a_1 = a_2 \simeq 0.85$ nm, $a_3 \simeq 0.45$ nm, and the refraction index $2.5 - 3$. The estimation of the exciton binding energy gives thus ca. 100 meV (at $\frac{\mu}{m\varepsilon^2} \sim 8 \times 10^{-3}$), as reported in [14]. For the averaged $q \sim 0.075 \times 2\pi/l$ (where $l \sim 0.5$ nm is taken to estimate the size of the Brillouin zone, and 0.075 taken as the averaged size of q on the Brillouin zone scale), the reducing of the exciton binding energy (at $\mu = 0.5m$, as in perovskite) is $\Delta E \sim 70$ meV, as measured by photoluminescence methods in the metalized perovskite cell [14].

3.2. Enhancement of light absorption, energy flow from plasmons to semiconductor substrate

In the case when metallic nanoparticles are deposited on the top of a semiconductor substrate, we deal with the energy transfer from plasmons oscillating in nanoparticles to a electron band system, causing interband transitions. This energy out-flow from plasmons causes their strong damping. The damping of plasmons is thus a measure of the efficiency of light absorption via plasmons.

To asses it quantitatively, let us assume that the energy inflow to the substrate semiconductor band system, $\mathcal{A}$, is equal to the outflow of energy from plasmons oscillating in metallic nanoparticles. Considering the gradual damping of plasmon oscillations according to the exponential lowering dipole amplitude, $D_0(t) = D_0 e^{-t/\tau'}$, we can estimate the transferred energy by the following formula (with δw given by Eq. (11)),

$$\mathcal{A} = \beta \int_0^\infty \delta w \hbar \omega dt = \beta \hbar \omega \delta w \tau'/2 = \begin{cases} \frac{2}{3} \frac{\beta \omega \tau' \mu \sqrt{m_n^* m_p^*}(\hbar\omega - E_g)e^2 D_0^2}{\hbar^4 \varepsilon^2}, & \text{for } a\xi \ll 1, \\ \frac{2}{3} \frac{\beta \omega \tau' \mu^{3/2}\sqrt{2}\sqrt{\hbar\omega - E_g}e^2 D_0^2}{a\hbar^3 \varepsilon^2}, & \text{for } a\xi \gg 1. \end{cases} \tag{27}$$

In the above formula the symbol τ' indicates the damping time-rate of surface plasmons coupled to the electrons in the semiconductor substrate, the parameter $\beta < 1$ accounts for all effects neglected but reducing transition probability, like deposition type, surface effects, irradiation losses in medium- and far-field zones. For nanoparticles radii $a \in (5, 100)$ nm the second limit in (27) is applicable. Via immediate comparison of $\mathcal{A}$ given by Eq. (27) with the initial energy of the plasmon oscillations which has been next transferred step-by-step to the semiconductor, one can find the damping rate, $\frac{1}{\tau'}$, for plasmons in the considered case. The initial energy of plasmons equals to [22], $\mathcal{B} = \frac{D_0^2}{2\varepsilon a^3}$. Assuming that $\mathcal{A} = \mathcal{B}$ we arrive with the formula for the damping rate for plasmons,

$$\frac{1}{\tau'} = \begin{cases} \frac{4\beta\omega\mu\sqrt{m_n^* m_p^*}(\hbar\omega - E_g)e^2 a^3}{3\hbar^4 \varepsilon}, & \text{for } a\xi \ll 1, \\ \frac{4\beta\omega\mu^{3/2}\sqrt{2}\sqrt{\hbar\omega - E_g}e^2 a^2}{3\hbar^3 \varepsilon}, & \text{for } a\xi \gg 1. \end{cases} \tag{28}$$

By τ' we denote here a large damping of plasmons due to the energy transfer to the semiconductor substrate highly exceeding the internal damping, characterized by τ, the latter due to the scattering of electrons inside the metallic nanoparticle [22] ($\frac{1}{\tau} \ll \frac{1}{\tau'}$). We neglect here also the irradiation to far-field upper hemisphere zone of the plasmon energy due to the Lorentz friction, which is also smaller than near-field zone energy transfer to the substrate [22]. For metal material of nanoparticles and the required parameters of semiconductors one can take the data from Tables 2, 3 and 4.

Knowing the damping rate of plasmons one can consider now a different scenario, when the out-flow of the plasmon energy is continuously recovered by income from the incident sun-light. In such a case we deal with the stationary state of a driven and damped oscillator for plasmons. Despite the free undamped plasmon has the Mie self-resonance frequency, $\omega_1 = \frac{\omega_p}{\sqrt{3}}$, the frequency of driven plasma oscillations equals to the driving electric field frequency, ω, i.e., the frequency of the incident e-m wave of photons. The continuous instant leakage of the plasmon energy to the semiconductor substrate, causes large damping of plasmon and the related red-shift and widening of the resonance, as usually for the damped and driven oscillator. The widened resonance allows for the energy transfer via plasmons to electrons at various frequencies limited, however, from below by the semiconductor forbidden gap $E_g/\hbar$.

Sun-light is not monochromatic and each its Fourier component is absorbed in an independent way. The electric field of incident e-m wave excites plasmons with the same frequency and such driven plasmons are damped with the rate $\frac{1}{\tau'}$ as given by Eq. (28). This damping causes a red-shift of the resonance and reduces the resonance amplitude, which in turn allows for the accommodation to the perfect balance of the energy transfer via plasmons of this particular Fourier component of sun-light. The amplitude of plasmon oscillations accommodated to such steady state of driven and damped oscillator, $D_0(\omega)$ is constant in time and given by the formula,

$$f(\omega) = \frac{1}{\sqrt{(\omega_1^2 - \omega^2)^2 + 4\omega^2/\tau'^2}}.$$

In the case of the energy balance one obtains according to Eq. (11) the following formula for the energy transfer mediated by plasmons at the stationary energy flow state,

$$q_m = \begin{cases} \beta C_0 \frac{128}{9} \pi^2 a^3 \frac{\mu \sqrt{\mu_n^* \mu_p^*}}{m^2} (\hbar\omega - E_g) \frac{e^6 n_e^2 \omega}{\hbar^4 \varepsilon^3} f^2(\omega), & \text{for } a\xi \ll 1, \\ \beta C_0 \frac{128}{9} \sqrt{2} \pi^2 a^2 \frac{\mu^{3/2}}{m^2} \sqrt{\hbar\omega - E_g} \frac{e^6 n_e^2 \omega}{\hbar^3 \varepsilon^3} f^2(\omega), & \text{for } a\xi \gg 1, \end{cases} \tag{29}$$

where, $f(\omega) = \frac{1}{\sqrt{(\omega_1^2 - \omega^2)^2 + 4\omega^2/\tau'^2}}$ corresponds to the amplitude factor for the driven damped oscillator and the dipole amplitude, $D_0 = \frac{e^2 n_e E_0 4\pi a^3}{3m} f(\omega)$ (in Eq. (11)). The amplitude of the electric field, E_0, of the incident e-m wave is next ruled out due to normalization per single photon; $C_0 = \frac{N_m 4/3\pi a^3}{V}$, V is the volume of the semiconductor, N_m is the number of metallic nanospheres.

One can write out the ratio, $\frac{q_m}{q_0}$, (where q_0 is the energy flow per single photon in ordinary photo-effect)—this ratio illustrates the advantage of the plasmon mediated photo-effect over the ordinary photo-effect and it attain the form,

$$\frac{q_m}{q_0} = \begin{cases} \frac{4\sqrt{2}\pi^2 a^3 \beta C_0 \sqrt{m_n^* m_p^*}(m_p^*)^2 e^4 n_e^2 \omega^2 f^2(\omega)}{3\mu^{3/2} m^2 \sqrt{\hbar\omega - E_g} \hbar \varepsilon^2}, & \text{for } a\xi \ll 1, \\ \frac{8\pi^2 a^2 \beta C_0 (m_p^*)^2 e^4 n_e^2 \omega^2 f^2(\omega)}{3\mu m^2 (\hbar\omega - E_g) \varepsilon^2}, & \text{for } a\xi \gg 1. \end{cases} \tag{30}$$

The enhancement of the electron interband transition probability induced by plasmons is linked with the admission of momentum-not-conserved transitions, which is, however, gradually reducing with the radius a growth. The strengthening of the near-field induced inter-band transitions, in the case of large nano-spheres, is, however, still significant as the quenching of oblique interband transitions is compensated by $\sim a^3$ growth of the amplitude of dipole plasmon oscillations. The nonlinear and nonmonotonous dependence on the radius a allows the trade-off between these two competing size-dependent factors and admit optimization of the plasmon mediated photo-effect (in agreement with experiments [9, 25, 26, 1, 27, 28]).

To verify the effectiveness of the plasmon mediated absorption one can estimate the photo-current in the semiconductor photodiode modified by metallic nanoparticles. The photo-current is given by,

$$I' = |e| N (q_0 + q_m) A,$$

where N is the number of incident photons and q_0 and q_m are the probabilities of single photon absorption in the ordinary photo-effect [29] and of single photon absorption mediated by the presence of metallic nano-spheres, respectively, $A = \frac{\tau_f^n}{t_n} + \frac{\tau_f^p}{t_p}$ is the amplification factor ($\tau_f^{n(p)}$ is the annihilation time of both sign carriers, $t_{n(p)}$ is the drive time for carriers [the time of traversing the distance between the electrodes]). We do not include here the presented formerly reduction of the exciton binding energy as we intend to assess here a net contribution of the absorption growth.

From the above formulae, we see that

$$\frac{I'}{I} = 1 + \frac{q_m}{q_0}, \tag{31}$$

where the ratio q_m/q_0 is given by Eq. (30) and $I = I'(q_m = 0)$, i.e., the photo-current without metallic modifications.

metal	Bulk pl [eV]	Surface pl [eV]
Li	6.6	3.4
Na	5.4	3.3
K	3.8	2.4
Mg	10.7	6.7
Al	15.1	8.8
Fe	10.3	5.0
Cu	6	3.5
Ag	3.8	3.5
Au	4.67	2.7

Table 2
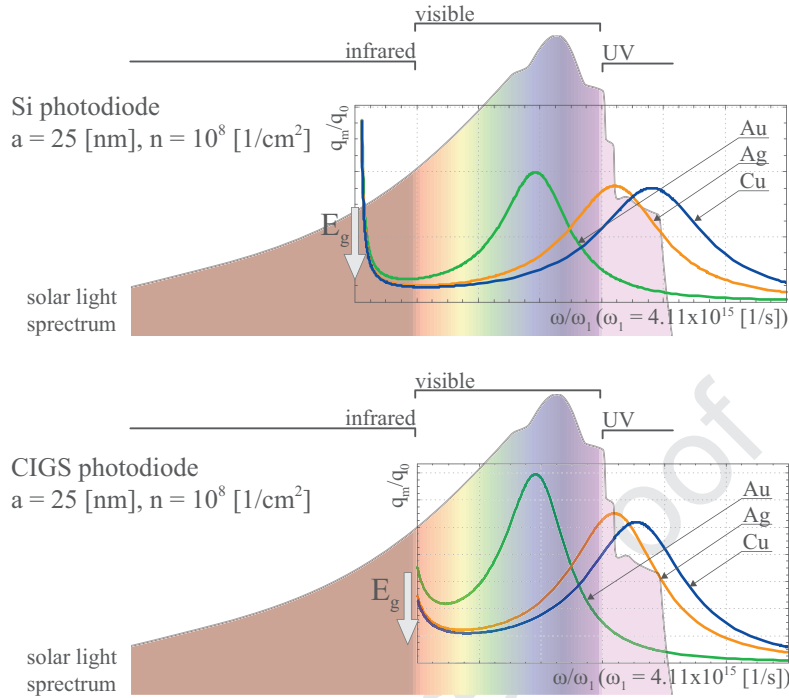Plasmon energies measured in metals

Figure 2: Comparison of the effectiveness of the plasmon channel expressed by $\frac{q_m}{q_0}(\omega)$ (cf. Eq. (30)) for the same substrate semiconductor Si (upper) and CIGS (lower) with Au (red), Ag (blue) and Cu (green) nanoparticles of the same radius 25 nm and the same surface density $10^8/cm^2$, versus the sun-light spectrum on the earth surface—the figure illustrates accommodation of the spectral characteristics of the plasmon mediated photo-effect, $\frac{q_m}{q_0}(\omega)$, to sun-light spectrum for different materials and covering parameters.

metal	Au	Ag	Cu
Mie frequency	4.11×10^{15} 1/s	5.2×10^{15} 1/s	5.7×10^{15} 1/s

Table 3
Mie frequency ω_1 to formula (30)

semiconductor	m_n^*	m_p^*	E_g
$CH_3NH_3PbI_3$	$1\ m$	$1\ m$	1.6 eV
Si	$0.9\ m$ L[101], $0.19\ m$ T[110]	$0.16\ m$ lh, $0.49\ m$ hh	1.12 eV
GaAs	$0.067\ m$	$0.08\ m$ lh, $0.45\ m$ hh	1.35 eV
CIGS	$0.09 - 0.13\ m$	$0.72\ m$	$1 - 1.7$ eV

Table 4
Substrate material parameters to formula (30) ($m = 9.1 \times 10^{-31}$ kg, the mass of bare electron; lh–light holes, hh–heavy holes, L–longitudinal, T–transverse)
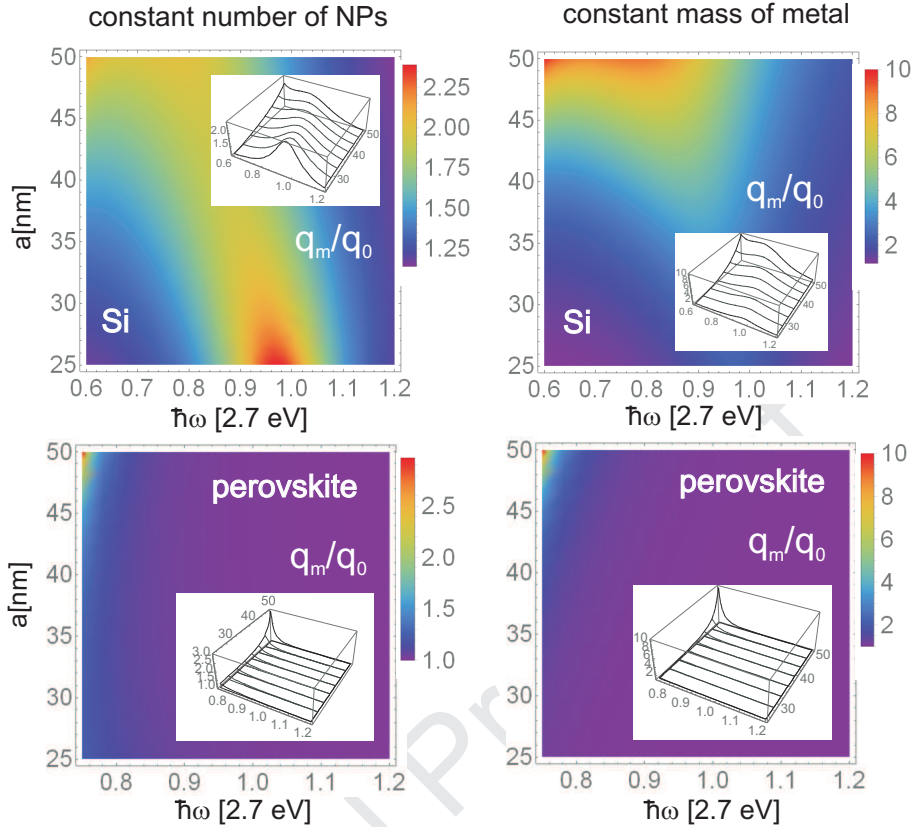
Figure 3: Spectral (with respect to ω) presentation of the efficiency increase $\frac{q_m}{q_0}$ (the ratio of probabilities of inter-band transitions per single photon with energy $\hbar\omega$ with and without metallic nanoparticles (NPs)—acc. Eq. (30)—including only absorption strengthening) for Si cell (upper) covered with bare Au NPs with radii $a \in 25 - 50$ nm. Similar spectral presentation of the efficiency increase $\frac{q_m}{q_0}$ for perovskite cell (lower) with core-shell NPs of the same size as for Si samples. Left panels correspond to kept constant concentration of NPs when their size is varying, whereas the right panels correspond to the total mass of all metallic components kept constant. The significant difference is noticeable—for perovskite cell, the metallic NPs almost do not enhance the efficiency in contrary to Si cell, which is the result of inconveniently large effective masses of carries in the perovskite and higher its forbidden gap in comparison to Si, entering the relation (30).

Strengthening of the absorption by mediation of plasmons very well describes the plasmon photovoltaic effect in $p - n$ junction-type cells. The agreement with photo-current measurements in laboratory Si diode setup metalized with various size Au nanoparticles is quantitative, both with respect to the photo-current enhancement rate (of order of 80% increase) and details of the spectral and size dependence [1, 12]. For complete Si-based solar cells the overall efficiency increase is lower because the absorption strengthening is only a first element in a long series of factors resulting in the cell efficiency, but the absorption strengthening agrees qualitatively with observations, cf. Table 1 and Figs 2, 3 [12, 21]. In Fig. 3 we compare the absorption strengthening in Si and perovskite by similar application of Au nanoparticles—the poor effect in perovskite is noticeable.

4. Metallization of perovskite solar cells

Plasmons cause modification both of photon absorption and of local electricity inside the cell metallically doped in nano-scale. Both these channels influence the overall efficiency of the cell with the ultimate efficiency enhancement being the subject of the trade-off between competing factors in dependence of material parameters and metallic nanoparticle size and deposition type. In the case of hybrid chemical perovskite cell the second channel, electrical one, occurs to be dominating which is confirmed experimentally [14] and predicted theoretically by assessment of the absorption channel—cf. Fig. 3. The electrical channel does not concern photon absorption strengthening by plasmons (which is poor in perovskite as shown in Fig. 3), but corresponds to strong decrease of binding energy of excitons

generated by the plasmon potential in its near field-zone. The lowering of exciton binding energy results in the easier dissociation of excitons at the surface of porous basis of the perovskite layer and in the eventual increase of a photo-current. The experimentally observed significant increase of the photo-current (but not of the voltage) and the eventual efficiency of the perovskite cell growth induced by metallic components is observed, cf. Fig. 4. The difference with the plasmon effect with the dominating channel of absorption growth (as in the case of Si cell covered by metallic nanoparticles on the cell top, or in other $p-n$ junction-type solar cells) reflexes different mechanisms of plasmon photovoltaic effect in perovskite and $p-n$ junction-type cells. The absorption channel causes an increase both of current and voltage as in Si case—cf. Fig. 5 (b,c), whereas the reducing of exciton binding energy strengthens the photo-current only—cf. Fig. 4 (c).
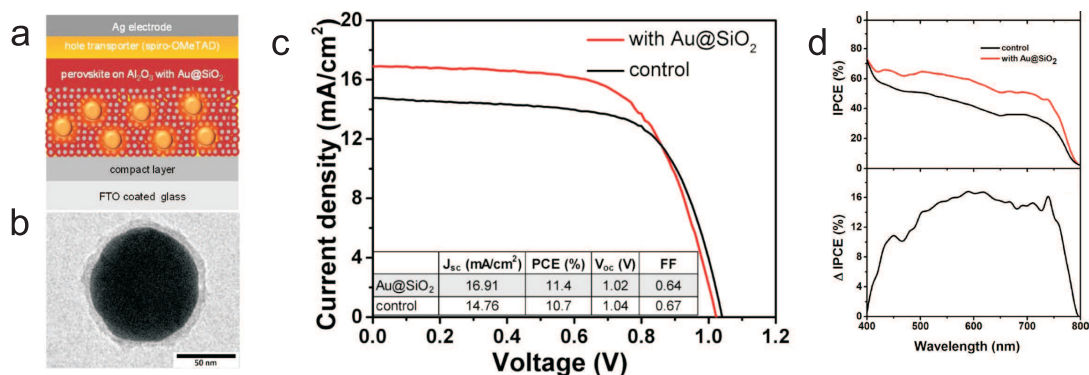

Figure 4: (a) Illustration of device structure with the component-layers indicated (b) TEM image of Au/SiO$_2$ core-shell NP ($a \sim 40$ nm, $b \sim 48$ nm—cf. Fig. 1 Inset. (c) I-V curve for perovskite cell with porous Al$_2$O$_3$ basis filled with Au/SiO$_2$ core-shell nanoparticles with density ~ 1 wt %; a strong increase of the photo-current is noticeably with simultaneous lowering of the voltage. (d) IPCE (photon-to-current conversion efficiency) spectra of control and with Au/SiO2 devices and its increase (ΔIPCE) due to the addition of Au/SiO$_2$ NPs (devices measured under AM1.5 simulated sunlight (100 mW/cm^2 irradiance). After experiment [14].
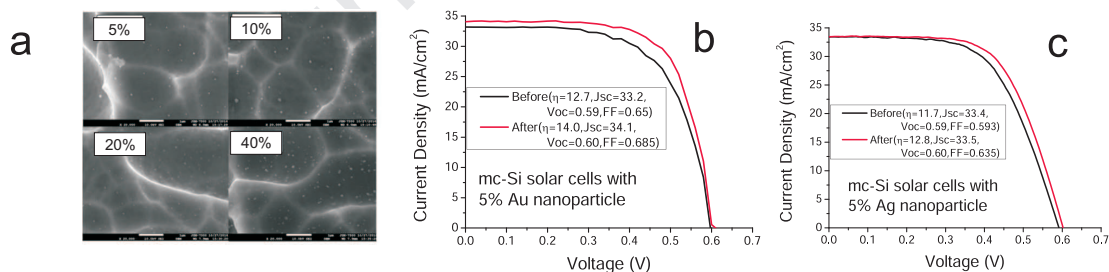

Figure 5: (a) Visualization by EM photography of distribution of metallic nanoparticles (Au) on the surface of the multi-crystalline Si solar cell under study for plasmonic effect as shown in (b); the very low surface concentration of metallic components is visible (percentage refers to concentration of colloidal solution used for spin coating of a cell surface). (b and c) Comparison of solar cell efficiency due to plasmon modification for the multi-crystal Si solar cell expressed by an increase of the area in the figure beneath the red I-V curve with respect to the area ranged by the black curve, (b) with photoactive surface modified by Au nanoparticles (efficiency increase is ca. 6.5%), (c) by Ag nanoparticles (efficiency increase is ca. 2.5%), acc. to our study [3]. The significant difference in I-V characteristic for metalized Si and perovskite cells is noticeable—compare Fig. 4(c)—which corresponds to different mechanism of plasmon induced efficiency increase, by strengthening of the photo-current due to easier dissociation of excitons in perovskite cell.

The perovskite solar cells utilizing the photo-active layer of CH$_3$NH$_3$PbX$_3$ with X = Cl, Br, and I are in the center of current photovoltaic research due to considerable advantages of high efficiency, low cost, easy low-temperature production and the compatibility with roll-to-roll (R2R) fabrication including screen or ink-jet printing. Even though the certificate efficiency of perovskite cells exceeds now 25% in single junction architecture (in silicon-based tandem

cells, up to 28%) [30, 31, 32, 33, 34, 35, 36, 37, 38], the further efficiency increase is desired to make perovskite compatible with the best Si cells. The easier way in this direction might be via the enhancement of the perovskite layer thickness to improve absorption rate of photons. This is, however, inconvenient because of parasitic increase of charge carrier recombination on longer distances for diffusion and the optimal thickness of the perovskite layer is $280 - 350$ nm [39, 40], which is low in comparison to major sun-light wavelengths and many photons left the structure. One can apply some modification like bottom mirror reflecting transmitted photons again to the active layer or a metallic plasmon hubs in the form of nanoparticles increasing photon absorption [16]. Authors of the paper [16] report 40% increase of the solar cell prototype, ITO/PEDOT:PSS/$CH_3NH_3PbI_3$/PCBM/Al doped with Au nanorods covered with silica SiO_2 layer—as shown in Figure 6. They achieved the increase of the overall cell efficiency form 10.9 % to 15.6 % (and even in a single sample, 17.6%), cf. Fig. 7. Core-shell metallic nanorods ae placed on the interface between PEDOT:PSS (50 nm thickness) and perovskite layer (290 nm thickness). The top of the structure has been coated with 30 nm of electron acceptor fullerene derivative PCBM and finally by Al 100 nm thick evaporated electrode. Au core of nanorods was of averaged size 15×40 nm and coated with ca. 9 nm thickness SiO_2 layer. The plasmon resonance of such nanorods is presented in Fig. 7. The dual surface plasmon resonance, longitudinal (ca. 700 nm) and transverse (ca. 520 nm) better accommodate to perovskite than the spherical nanoparticle single resonance, taking into account the forbidden gap value (ca. 1.6 eV, i.e., 770 nm). Positioning of metallic core-shell nanorods on the interface with hole absorber PEDOT:PSS suggests that dissociation of excitons is of high importance to accelerate capturing of holes (similarly as capturing of electrons in the interface between perovskite and TiO_2 or Al_2O_3 in the alternative architecture of the perovskite cell [14]). The larger increase of the photocurrent than of voltage observed in the experiment [16] suggest that the contribution of this channel of plasmonic effect is significant here (cf. Fig. 7). However, some small shift in voltage (visible in Fig. 7) evidences also contribution of the plasmon induced photon absorption. It must be emphasized that this increase is not only due to local concentration of the electrical field close to the curvature of nanoparticles (as shown in the Appendix C) but also due to breaking of the translational symmetry and admittance of nonvertical interband transitions as described in previous paragraphs. The impressive increase (40%) of the efficiency of considered in [16] perovskite cell indicates a great potential of the metallization toward the increase of the cell efficiency, by the nanoparticle deposition and shape engineering to optimize the accommodation to plasmon photovoltaic channels.
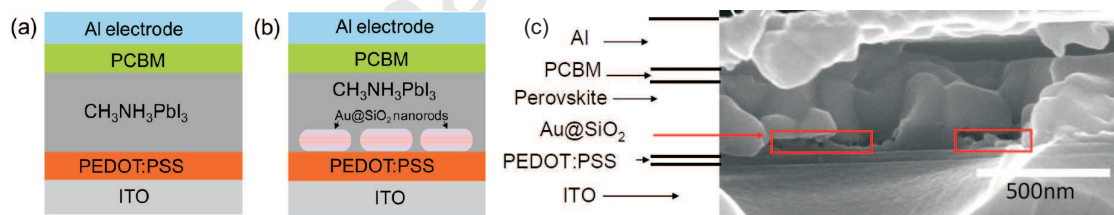

Figure 6: Perovskite device layers with (b) and without (a) Ag@SiO$_2$ nanorods; the lateral SEM image (c) of the layered structure with Au@SiO$_2$ nanorods clustered and embedded at the interface between the PEDOT:PSS layer and the perovskite layer, after [16].
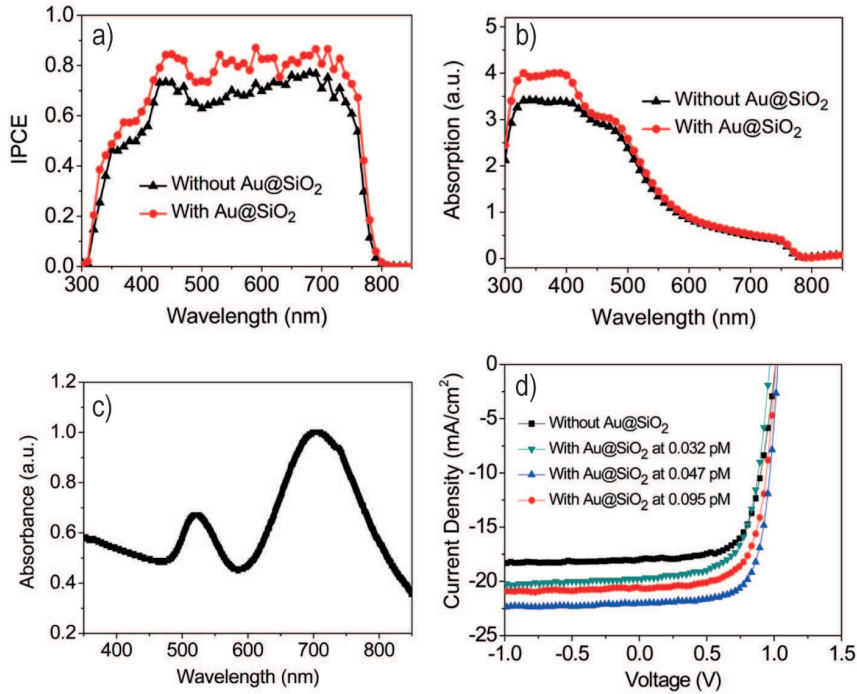
Figure 7: The enhancement of the efficiency of perovskite solar cell metalized by nanorods, as shown in Fig. 7 (a); the measured absorption increase in the same device (b)—by the comparison of (a) and (b) it is visible that the absorption increase appears between 300 and 450 nm for wavelength only, thus the increase of the efficiency between 450 and 800 nm is due to non-optical (electrical) effect; the double plasmon resonance in the nanorod corresponding to longitudinal and transverse polarization modes (c); the increase of the efficiency of the perovskite cell metalized by nanorods for various concentration of nanorods—the best one is for a medium concentration of nanorods, 0.047 pM (dilution of nanorod colloidal solution utilized for the deposition by spin-coating-method) (d), after [16].

In experimental studies of metallic plasmonic components in solar cells, as a factor causing the photovoltaic efficiency increase is considered only the concentration of electric field near the metallic nanoparticle curvature, cf. e.g., [14, 15, 16]. Experimenters give only qualitative arguments, which are, however, strongly inaccurate. As has been demonstrated [21], the concentration of the electric field explains at most only 10% of the plasmonic strengthening of absorption, whereas 90% of the increase is linked with quantum corrections changing the dielectric functions of metallic nanoparticle and of the semiconductor substrate (cf. illustration in Appendix D). Coupling of plasmons to band electrons creates a fast and efficient channel for energy transfer, which strongly modifies the damping of plasmons and the absorption of semiconductor band electrons far beyond the only increase caused by the local field concentration. While the latter can be found by the solution of Maxwell-Fresnel equations with boundary conditions on the interface of nanoparticle metal with surrounding semiconductor, much more important quantum effect must be included beyond the classical approach by application of the Fermi golden rule applied to the plasmon coupling with band electrons [12, 21]. The related enhancement of the light absorption prevails by at least one order of magnitude over the effect caused by field strengthening solely (as shown in Appendix D for Si semiconductor substrate [21]).
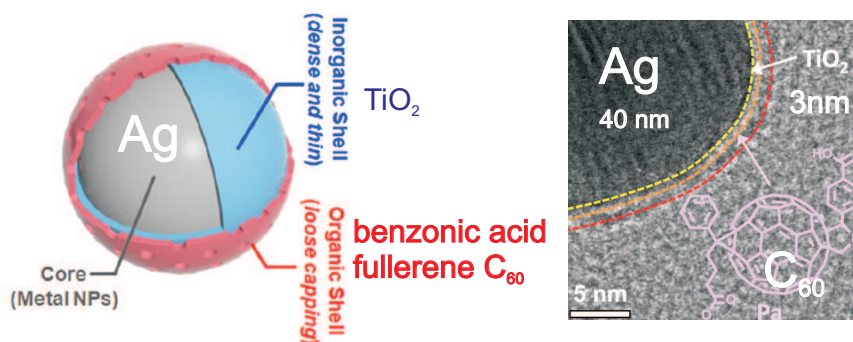
Figure 8: Bi-shell-core metallic component Ag@TiO$_2$@organic shell (left) and its HRTEM image (right); the chemical structure of organic molecule is presented, after [15].

The same can be addressed also to perovskite cells, where the strong increase of the efficiency was by experimenters also linked with concentration of the electrical field and only phenomenologically named as the optical and electrical influence [15]. In the former paragraphs we addressed these two general notions within the microscopic treatment of the plasmon to electron coupling upon the Fermi golden rule scheme and we have found quantitatively factors responsible both for optical and electric influence of plasmons in nanoparticles contributing together to plasmon photovoltaic effect.
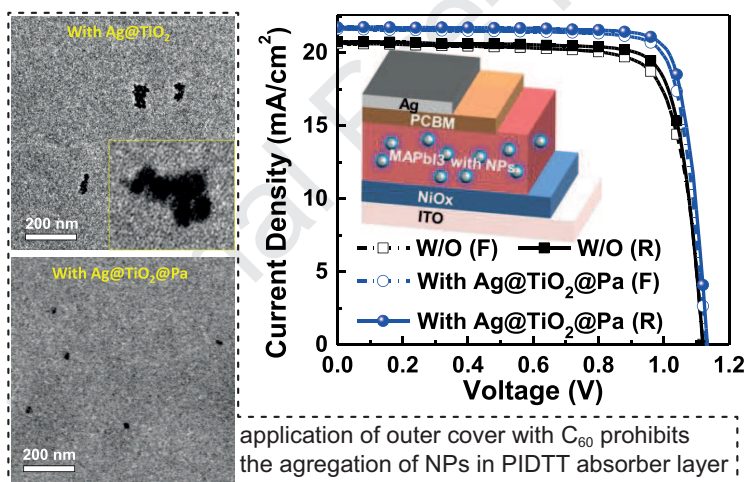

Figure 9: (left) TEM images of a PIDTT-DFBT:PC71BM film incorporated with Ag@TiO$_2$ or Ag@TiO$_2$@Pa (Pa is the organic shell of benzoic acid fullerene C$_{60}$)—the prohibition against nanoparticle aggregation in PIDTT absorber layer is visible. (right) Increase of the efficiency of solar cell (the device presented in Inset) with and without metallic bi-shell-core nanoparticles (R and F indicate reverse (from V to J) and forward scan (from J to V), respectively), after [15].

Such microscopic specification of the plasmon photovoltaic effect is helpful in better identification of the ways for optimization of this effect via selection of the material, size, shape, and the deposition type in a more predictable and controllable manner. The abundance of experimental tests of different materials and parameters, via the trial and error method, offers the large domain for verification of the theory and, in turn, for better focusing of further attempts. For example, in the paper [15] the double-core-shell metallic nanoparticles have been utilized—Ag@TiO$_2$@Pa (i.e., Ag nanoparticles decorated with a titania and benzoic-acid-fullerene C$_{60}$—cf. Fig. 8). The choice of Ag instead of more conventional Au for metallic core material founds support in plasmon resonance in Ag blue-shifted in comparison to Au, which is convenient for perovskite where the red/infrared part of the solar-light spectrum is cut out by the relatively large forbidden gap in perovskite (ca. 1.6 eV, i.e., ca. 770 nm) and in Ag plasmon resonance better suits to perovskite than Au resonance (though the latter was more convenient in Si—cf. Appendix B). The dielectric cover may play the double role—from one side, it slightly red-shifts the plasmon resonance (cf. Appendix B, which is, however, unimportant for thin dielectric layer, cf. Fig. 8), and from other side, this layer isolates the metal form the carries in

the semiconductor medium preventing their recombination and the lowering of the final photo-current. The benzoic acid fullerene outer layer is believed to play a role to better adjust the admixture to surroundings (to be compatible of nanoparticles with the fullerene acceptors or perovskite absorber in layers of which nanoparticles are embedded [15]) and in this way to avoid destruction of the layer structure morphology. Such a multi-direction design of plasmon components takes into account various competing factors but all only at the phenomenological qualitative level. Thus, the more precise theoretical assessment of some of these factors seems to be an important supplement for the cell metallization engineering.

For high efficiency and improved durability of perovskite cells the homogeneity of the perovskite layer is important. Although rapid deposition of large-area perovskite films under ambient conditions is an important goal in photovoltaics, rapid crystallization at low temperatures generally results in poor quality films with many defects that are not suitable for solar cell applications, so a slow growth and high temperature annealing are commonly used. The metallization of the cell by nanoparticles utilizing liquid precursors of the perovskite with blended colloidal solution of metallic nanoparticles would additionally worsen crystallization and nucleation process and disturb final morphology of layers. To overcome these obstacles the multilayer coatings of metallic nanoparticles are proposed to prohibit the aggregation of embedded particles [15], or the deposition of metallic components by spinning coating onto the substrate layer before application of the perovskite precursors [14] or after crystallization of the perovskite layer, in the inverted architecture [16]. The spinning coating is, however, not suitable for large-area deposition [14] and can be utilized for manufacturing laboratory small test samples only. To avoid this limit some in air-puff sputtering of metallic nanoparticle dust via additional head at ink-jet printing deposition might be helpful before print of the perovskite or after its crystallization (the same may be applied at large scale screen-print technique). The new technology advances to improve homogeneity of perovskite layer by so-called pre-nucleation technique has been also reported [41]. Compared to traditional solvent dripping methods, the approach enables the creation of smaller crystallites in the perovskite films to avoid uncontrolled crystallite growth worsening the efficiency and durability of cells. Unlike the conventional method of solvent dripping in ambient air, which leads to large intermediate crystals, the method proposed to deliver smaller crystals in the wet films which are easier to convert into perovskite which would be conveniently associated with nano-metallization.

The range of the near-field coupling of plasmons in metallic nanoparticles with excitons in a semiconductor is proven experimentally to be not lower than 1 micrometer [10]. This has been demonstrated by separation of Ag nanoparticles from the photoactive semiconductors by of 1 micrometer height thin (300 nm) nano-columns of ZnO covered next with nanoparticles from above and still observation of the plasmon photovoltaic effect in the bottom substrate despite the spatial separation [10]. In perovskite solar cells the optimal thickness of the active semiconductor layer is ca. 300 nm (to avoid recombination losses in thicker layers) [39, 40], thus blending metallic nanoparticles into the electron or hole transport layer will cause similar plasmon effect to that one if nanoparticles are embedded in the perovskite layer. However, in the case of inverted cell structure with PEDOT:PSS as the hole transporter, its layer is also very fragile and unstable [16] and similarly for PIDTT absorber [15], and to avoid layer morphology perturbations by metallic components the special outer organic coating of nanoparticles appeared to be needed to apply (as shown in Figs 8 and 9) [15]. Optimal localization of the metallic components is on the interface between the absorber layer and perovskite layer, close to the region where excitons are decoupling (releasing electrons or holes to the transporter depending on cell configuration), but in the way which minimizes structural defects in adjacent layers. One can expect that pneumatic puff-dust controlled deposition of metallic nanoparticles during appropriately tailored ink-jet printing would be the prospective method.

Moreover, the methods of perovskite cell production are still developing, which opens new possibilities to perform metallization with nanoparticles. The interesting new method allows for the deposition of large-area, high-quality perovskite films under mild conditions by designed a general solvent mixing so that one can blade-coat continuous, large grain and compact perovskite films at unprecedented speed (10 cm/s) at room temperature in air. The observation that some mixed composition of reaction substrates resulting in non-perfect homogeneity of perovskite layer occurred to be surprising. It has been discovered that that rough multi-component alloyed preparations were actually improving the efficiency of the materials by creating lots of areas with different compositions that could trap the energized charge carriers. Companies looking to make bigger fabrication lines for perovskites have been trying to solve the problem of how to make the films more homogeneous, but now it has been shown them that actually a simple ink-jet printing process could induce some disorder in the materials to help the achievement of maximum efficiency. By mixing bromine and indium in liquid precursors, the researchers were able to defeat defects in the material [42, 43]. Another important factor is the degradation problem known as light-induced phase-segregation, which occurs when the alloys that make up the solar cells break down under exposure to continuous light. Perovskite solar cells are typically made

using a combination of iodine and bromine, or bromine and chlorine, but the researchers improved upon the formula by including all three types of halides. Adding chlorine to iodine and bromine created a triple-halide perovskite phase and suppressed the light-induced phase-segregation [44].

5. Conclusion

The microscopic theory of plasmon photovoltaic effect has been developed embracing both optical and electrical channels of plasmon mediation in enhancement of solar cell efficiency by metallization. By application of the Fermi golden rule scheme we have demonstrated how the efficiency of the energy transfer channel between the surface plasmon oscillations in a metallic nanoparticles and a substrate semiconductor depends on parameters of both deposited metallic particles (its radius and composition) and on semiconductor parameters (energy gap, and effective masses of electrons and holes). The formula found in analytical form generalizes the ordinary photo-effect onto the plasmon mediated one, quantitatively agrees with the experimental measurements in a laboratory photo-diode configurations. The qualitative agreement has been demonstrated also for complete solar cells where the plasmon absorption effect is obscured by other elements of the long series of effects resulting in overall solar cell efficiency besides the absorption of photons only. Complementary to absorption effect we described also the plasmon electrical mechanism especially important in chemical and hybrid perovskite cells with exciton pattern of operation. Both channels of plasmon effect, optical and electrical, cause independently a significant increase of the cell efficiency (the record of 40%) and the realistic microscopic model can supplement the experimental trial and error method. The opinion that plasmon effect takes advantage of electric field concentration near nanoparticle curvature occurred misleading as more than 90% of eventual efficiency increase due to plasmons is caused by quantum effects out of reach conventional Maxwell-equation-plasmonics.

Better adjustment of the plasmon resonance in metallic multi-shell non-spherical components to a particular cell device is possible by utilization of presented theory for metallization engineering. Perovskite cells, chemical, plastic and hybrid ones are especially sensitive to metallization because allows for development of both channels of plasmon effect in contrary to conventional $p - n$ junction cells. This is of high importance because the third generation cells achieve (as perovskite cells) the efficiency comparable to $p - n$ junction cells and additional large (up to 40%) increase of their operation efficiency by low cost metallization, at low temperatures and easy technology makes them competing solution for future large scale applications.

Acknowledgmets

A. Analytical calculation of integrals in Eq. (10)

The potential for the near-field interaction of the surface Mie type plasmons with the band electrons can be written as [23]:

$$
\begin{aligned}
w &= e\psi(\mathbf{R}, t) = \frac{e}{\varepsilon_0 R^2}\hat{\mathbf{n}} \cdot \mathbf{D}_0 sin(\omega t + \alpha) = w^+ e^{i\omega t} + w^- e^{-i\omega t}, \\
w^+ &= (w^-)^* = \frac{e}{\varepsilon_0 R^2}\frac{e^{i\alpha}}{2i}\hat{\mathbf{n}} \cdot \mathbf{D}_0
\end{aligned}
\tag{32}
$$

and the inter-band transition probability is given by the Fermi golden rule,

$$
w(\mathbf{k}_1, \mathbf{k}_2) = \frac{2\pi}{\hbar}\left| < \mathbf{k}_1|w^+|\mathbf{k}_2 > \right|^2 \delta(E(\mathbf{k}_1) - E(\mathbf{k}_2) + \hbar\omega),
\tag{33}
$$

where the Bloch states in the conduction and valence bands we assume as planar waves (for the sake of simplicity),

$$
\begin{aligned}
\Psi_{\mathbf{k}_1} &= \frac{1}{(2\pi)^{3/2}}e^{i\mathbf{k}_1 \cdot \mathbf{R} - iE_p(\mathbf{k}_1)t/\hbar}, \Psi_{\mathbf{k}_2} = \frac{1}{(2\pi)^{3/2}}e^{i\mathbf{k}_2 \cdot \mathbf{R} - iE_n(\mathbf{k}_2)t/\hbar}, \\
E_p(\mathbf{k}_1) &= -\frac{\hbar^2\mathbf{k}_1^2}{2m_p^*} - E_g, E_n(\mathbf{k}_2) = \frac{\hbar^2\mathbf{k}_2^2}{2m_n^*},
\end{aligned}
\tag{34}
$$

(indices n, p refer to electrons from the conduction and valence bands, respectively, E_g is the forbidden gap).

To calculate the matrix element,

$$< \mathbf{k}_1 | w^+ | \mathbf{k}_2 > = \frac{1}{(2\pi)^3} \int d^3 R \frac{e}{\varepsilon_0 2i} e^{i\alpha} \hat{\mathbf{n}} \cdot \mathbf{D}_0 \frac{1}{R^2} e^{-i(\mathbf{k}_1 - \mathbf{k}_2) \cdot \mathbf{R}}, \tag{35}$$

let us introduce the vector $\mathbf{q} = \mathbf{k}_2 - \mathbf{k}_1$. One can choose the coordinate system in such a way, that the vector $\mathbf{q}$ is oriented along the z axis, and the vector $\mathbf{D}_0$ lies in the plane zx (as is depicted in Fig. 10).
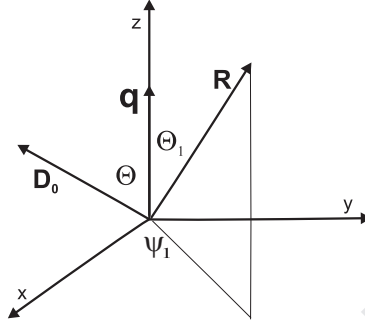
Figure 10: The reference frame is chosen in the way that the vector $\mathbf{q}$ is oriented along the axis z, while the vector $\mathbf{D}_0$ lies in the plane xz

Then, $\mathbf{q} = (0, 0, q)$, $\hat{\mathbf{n}} = \frac{\mathbf{R}}{R} = (sin\Theta_1 cos\psi_1, sin\Theta_1 sin\psi_1, cos\Theta_1)$, $\mathbf{R} = R(sin\Theta_1 cos\psi_1, sin\Theta_1 sin\psi_1, cos\Theta_1)$, $\mathbf{D}_0 = D_0(sin\Theta, 0, cos\Theta)$ and

$$\mathbf{q} \cdot \mathbf{R} = qR cos\Theta_1, \tag{36}$$

$$\hat{\mathbf{n}} \cdot \mathbf{D}_0 = D_0(sin\Theta sin\Theta_1 cos\psi_1 + cos\Theta cos\Theta_1). \tag{37}$$

Hence,

$$\begin{aligned}
&< \mathbf{k}_1 | w^+ | \mathbf{k}_2 > \\
&= \frac{1}{(2\pi)^3} \int d^3 R \frac{e}{\varepsilon_0 2i} e^{i\alpha} \hat{\mathbf{n}} \cdot \mathbf{D}_0 \frac{1}{R^2} e^{-i(\mathbf{k}_1 - \mathbf{k}_2) \cdot \mathbf{R}} \\
&= \frac{1}{(2\pi)^3} \frac{ee^{i\alpha}}{\varepsilon_0 2i} D_0 \int_a^\infty \frac{R^2}{R^2} dR \int_0^\pi \\
&\times sin\Theta_1 d\Theta_1 \int_0^{2\pi} d\psi_1 \{cos\Theta cos\Theta_1 + sin\Theta sin\Theta_1 cos\psi_1\} e^{iqR cos\Theta_1} \\
&= \frac{1}{(2\pi)^3} \frac{ee^{i\alpha}}{\varepsilon_0 2i} D_0 cos\Theta 2\pi \int_a^\infty dR \int_0^\pi cos\Theta_1 sin\Theta_1 d\Theta_1 e^{iqR cos\Theta_1},
\end{aligned} \tag{38}$$

the integer over $d\psi_1$ vanishes the second term in the parenthesis and only the first term contributes with the factor 2π. Note that,

$$\int_0^\pi cos\Theta_1 sin\Theta_1 d\Theta_1 e^{ix cos\Theta_1} = -i\frac{d}{dx} \int_0^\pi sin\Theta_1 e^{ix cos\Theta_1} = -i\frac{d}{dx} 2\frac{sinx}{x}. \tag{39}$$

Thus,

$$\begin{aligned}
&< \mathbf{k}_1 | w^+ | \mathbf{k}_2 > = \frac{-1}{(2\pi)^3} \frac{ee^{i\alpha}}{\varepsilon_0} D_0 cos\Theta(2\pi) \int_a^\infty dR \frac{1}{q} \frac{d}{dR} \frac{sinqR}{qR} \\
&= \frac{1}{(2\pi)^2} \frac{ee^{i\alpha}}{\varepsilon_0} D_0 cos\Theta \frac{1}{q} \frac{sinqa}{qa} \rightarrow_{a \to 0} \frac{1}{(2\pi)^2} \frac{ee^{i\alpha}}{\varepsilon_0} D_0 cos\Theta \frac{1}{q}.
\end{aligned} \tag{40}$$

Now we will integrate over all initial and final states of both bands. The related integration over $\mathbf{k}_1, \mathbf{k}_2$, one can substitute with integration over $\mathbf{q}, \mathbf{k}_2$. Scalar products are invariant against coordinate systems rotations, therefore the result of integration will be the same if $\mathbf{q}$ was along z axis or $\mathbf{D}_0$ is oriented now along the z axis—Θ gives, in the latter case, the deviation of $\mathbf{q}$ with respect to z direction – this choice of the reference frame is convenient for integration with respect to $d\mathbf{q}$. The transition probability has the following form,

$$\delta w = \int d^3 k_1 \int d^3 k_2 \left[f_1(1 - f_2) w(\mathbf{k}_1, \mathbf{k}_2) - f_2(1 - f_1) w(\mathbf{k}_2, \mathbf{k}_1) \right], \tag{41}$$

where f_1, f_2 assign the temperature dependent distribution functions (Fermi-Dirac distribution functions) for initial and final states, respectively. At room temperatures, $f_2 \simeq 0$ and $f_1 \simeq 1$, which leads to,

$$\delta w = \int d^3 k_1 \int d^3 k_2 w(\mathbf{k}_1, \mathbf{k}_2). \tag{42}$$

In the above formula we avoided the density state factors canceled by the probability re-normalization.

We have to calculate the following integral,

$$\delta w = \int d^3 k_2 \int d^3 q \frac{e^2}{(2\pi)^3 \hbar \varepsilon_0} \frac{D_0^2 cos^2 \Theta}{q^2} \frac{sin^2(qa)}{(qa)^2} \delta \left(\frac{\hbar^2 k_1^2}{2m_n^*} + \frac{\hbar^2 k_2}{2m_p^*} - (\hbar\omega - E_g) \right), \tag{43}$$

with $\delta \left(\frac{\hbar^2 k_1^2}{2m_n^*} + \frac{\hbar^2 k_2}{2m_p^*} - (\hbar\omega - E_g) \right) = \frac{1}{\alpha+\beta} \frac{1}{2\beta' q k_2} \delta \left(cos\Theta_2 - \frac{k_2^2 + \beta' q^2 - \gamma'}{2\beta' q k_2} \right)$, where, $\alpha = \frac{\hbar^2}{2m_n^*}$, $\beta = \frac{\hbar^2}{2m_p^*}$, $\gamma = \hbar\omega - E_g$, $\alpha' = \frac{\alpha}{\alpha+\beta}$, $\beta' = \frac{\beta}{\alpha+\beta}$, $\gamma' = \frac{\gamma}{\alpha+\beta}$. For each integral, with respect to $\mathbf{k}_2$ and $\mathbf{q}$ the coordinate system can be rotated independently, and for integration over $d\mathbf{k}_2$ we choose again orientation of $\mathbf{q}$ along the axis z, which leads to the spherical angle Θ_2 resulting from the product, $\mathbf{k}_2 \cdot \mathbf{q} = k_2 q cos\Theta_2$.

The expression for δw attains thus the form,

$$\delta w = \frac{e^2 D_0^2}{(2\pi)^3 \hbar \varepsilon_0^2} \int d^3 q \frac{sin^2(qa)}{q^2 a^2} \frac{cos\Theta}{q^2}$$
$$\int_0^\infty dk_2 k_2^2 \int_0^\pi d\Theta_2 sin\Theta_2 \int_0^{2\pi} d\psi_2 \frac{1}{\alpha+\beta} \frac{1}{2\beta' q k_2} \delta \left(cos\Theta_2 - \frac{k_2^2 + \beta' q^2 - \gamma'}{2\beta' q k_2} \right). \tag{44}$$

Integration over $d\Theta_2$ employs the Dirac delta. The relevant nonzero contribution (due to integration over $dcos\Theta_2$) is conditioned by the inequality,

$$-1 < \frac{k_2^2 + \beta' q^2 - \gamma'}{2\beta' q k_2} < 1, \tag{45}$$

which resolves itself to the constraint,

$$\left| \beta' q - \sqrt{\gamma' - (1-\beta')\beta' q^2} \right| < k_2 < \beta' q + \sqrt{\gamma' - (1-\beta')\beta' q^2}. \tag{46}$$

Thus,

$$\delta w = \frac{1}{(\alpha+\beta)2\beta'} \frac{e^2 D_0^2}{2\pi \hbar \varepsilon_0^2} \int_0^{\sqrt{\frac{\gamma'}{\beta'(1-\beta')}}} dq q^2 \frac{sin^2 qa}{(qa)^2}$$
$$\times \int_0^\pi d\Theta sin\Theta cos^2\Theta \frac{1}{q^3} \int_{|\beta' q - \sqrt{\gamma' - (1-\beta')\beta' q^2}|}^{\beta' q + \sqrt{\gamma' - (1-\beta')\beta' q^2}} dk_2 k_2. \tag{47}$$

and hence,

$$\delta w = \frac{2}{3} \frac{\sqrt{\gamma'}}{\alpha+\beta} \frac{e^2 D_0^2}{2\pi \hbar \varepsilon_0^2} \frac{1}{\zeta} \int_0^1 dx \frac{sin^2(x(a/\zeta))}{(x)^2(a/\zeta)^2} \sqrt{1 - x^2}, \tag{48}$$

where, $\zeta = \sqrt{\frac{(1-\beta')\beta'}{\gamma'}}$. Therefore,

$$\delta w = \frac{4}{3} \frac{\mu^2 (m_n^* + m_p^*) 2(\hbar\omega - E_g) e^2 D_0^2}{\sqrt{m_n^* m_p^*} 2\pi \hbar^5 \varepsilon_0^2} \int_0^1 dx \frac{sin^2(xa/\zeta)}{(xa/\zeta)^2} \sqrt{1 - x^2}$$
$$= \frac{4}{3} \frac{\mu^2}{\sqrt{m_n^* m_p^*}} \frac{e^2 D_0^2}{2\pi \hbar^3 \varepsilon_0^2} \xi^2 \int_0^1 dx \frac{sin^2(xa\xi)}{(xa\xi)^2} \sqrt{1 - x^2}, \tag{49}$$

where, $\xi = 1/\zeta = \frac{\sqrt{2(\hbar\omega - E_g)(m_n^* + m_p^*)}}{\hbar}$.

In limiting cases, we obtain finally,

$$
\delta w = \begin{cases} \dfrac{1}{3} \dfrac{\mu^2 (m_n^* + m_p^*) 2(\hbar\omega - E_g) e^2 D_0^2}{\sqrt{m_n^* m_p^*} 2\hbar^5 \varepsilon_0^2}, & a\xi \ll 1, \\[3mm] \dfrac{4}{3} \dfrac{\mu^2 (m_n^* + m_p^*) 2(\hbar\omega - E_g) e^2 D_0^2}{\sqrt{m_n^* m_p^*} 4 a\xi \hbar^5 \varepsilon_0^2}, & a\xi \gg 1, \end{cases}
\tag{50}
$$

In the latter case the following approximation was applied,

$$
\int_0^1 \frac{sin^2(xa\xi)}{(xa\xi)^2} dx \approx (for \; a\xi \gg 1) \frac{1}{a\xi} \int_0^\infty d(xa\xi) \frac{sin^2(xa\xi)}{(xa\xi)^2} = \frac{\pi}{2a\xi},
$$

while in the former one, $\int_0^1 dx \sqrt{1 - x^2} = \pi/4$.

The result must be multiplied by 4 (due to spin). In the considered limiting cases we obtain thus,

$$
\delta w = \begin{cases} \dfrac{4}{3} \dfrac{\mu \sqrt{m_n^* m_p^*}(\hbar\omega - E_g) e^2 D_0^2}{\hbar^5 \varepsilon_0^2} \; for \; a\xi \ll 1, \\[3mm] \dfrac{4}{3} \dfrac{\mu^{3/2} \sqrt{2} \sqrt{\hbar\omega - E_g} e^2 D_0^2}{a\hbar^4 \varepsilon_0^2} \; for \; a\xi \gg 1, \end{cases}
\tag{51}
$$

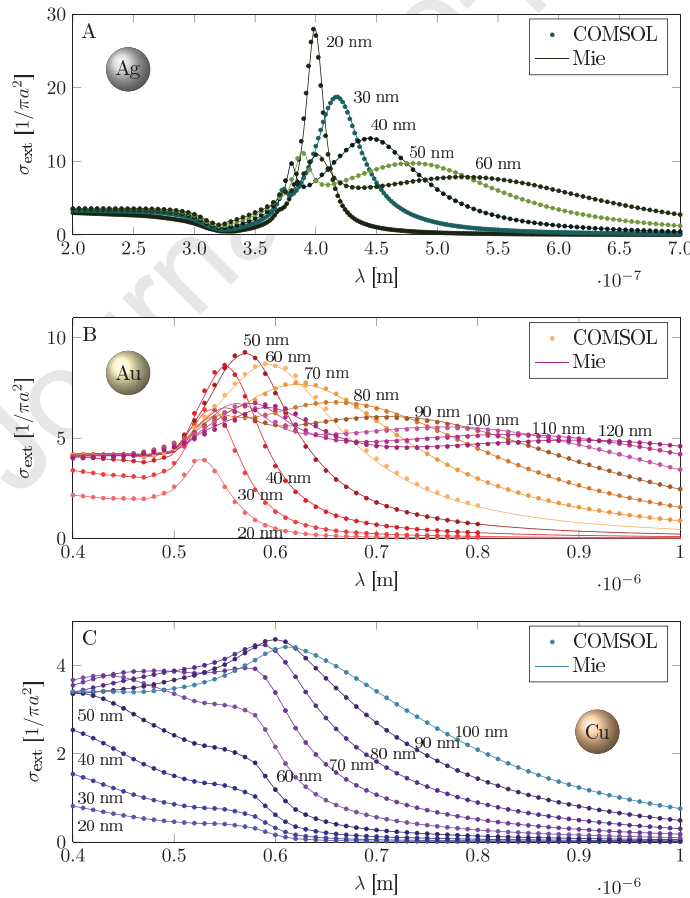(the formula is addressed to the case of the completely embedded nanosphere).

Figure 11: Surface plasmon resonances (extinction cross-section $\sigma_{ext}(\lambda)$ spectral dependence) for Au, Ag and Cu spherical nanoparticles with various radii. The dominating peak corresponding to the dipole plasmon mode at the radii region $a \in (10 - 100)$ nm very well overlaps with the visible part of the sun-light spectrum, which is convenient for plasmon-photovoltaic applications.
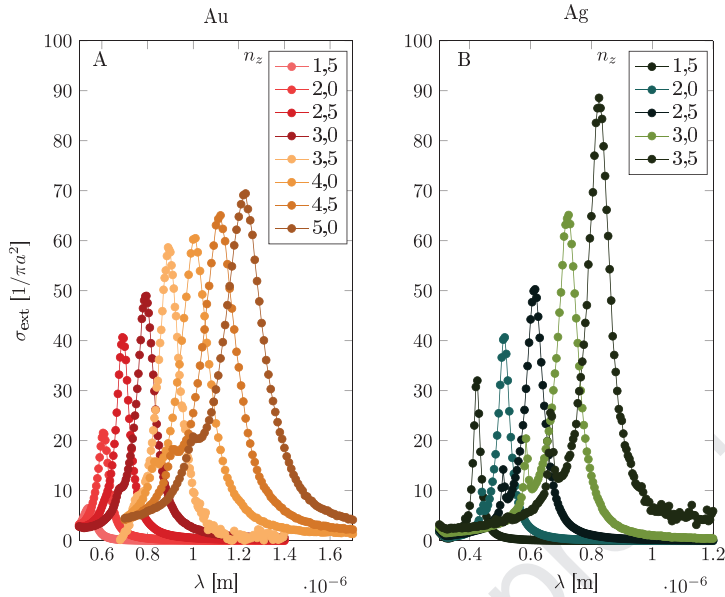
Figure 12: The dependence of the surface plasmon resonance (extinction cross-section spectral dependence) with respect to the permittivity $\varepsilon = n_z^2$ of the dielectric surroundings (n_z is the refraction index of the dielectric medium, as marked in the figure). The dependence is relatively strong and in the figure shown for Au and Ag nanoparticles with radius $a = 20$ nm.
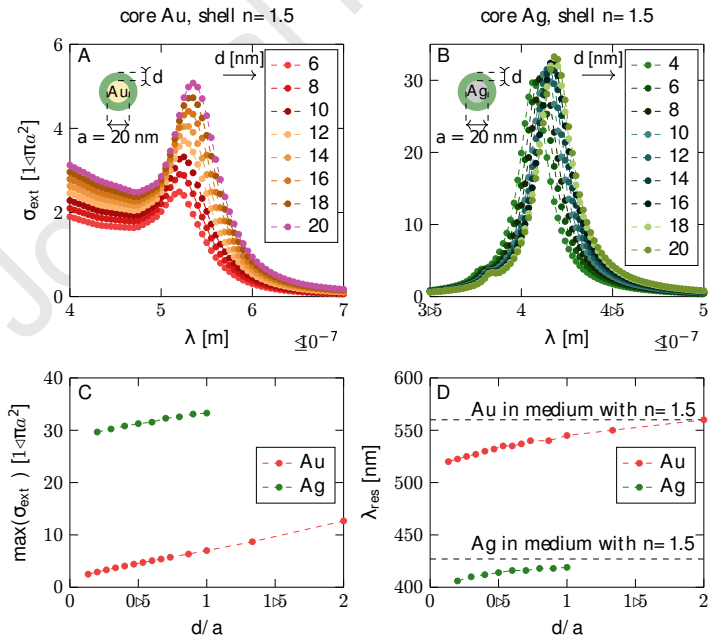

Figure 13: Red shift of the surface plasmon resonance (extinction cross-section spectral dependence) in metallic spherical core with respect to the thickness of the dielectric coating layer, d (for core Au (A), Ag (B)). In the figure the size dependence is presented for Au and Ag spherical cores with constant radii $a = 20$ nm with respect to the coating thickness d with the dielectric of permittivity $\varepsilon = n^2 = 2.25$—maximal extinction cross-section (C) and central resonance wave length (D).

B. Characterization of plasmon resonances in shell-core metallic nanoparticles

In Fig. 11 we present the surface plasmon resonances in nanoparticles of Au, Ag and Cu. Differences in position of maxima of resonances versus the solar light spectrum and the cut off by the forbidden gap in the semiconductor substrates favor different metal materials for specific devices, e.g., in perovskite solar cells an application of Ag core nanoparticles enhances the absorption [15], which was poor for Au cores [14], because of relatively large forbidden gap in perovskite and cutting off the red/infra-red sun-light spectrum.

Moreover, by application of thicker dielectric shells one can precisely accommodate the plasmon resonance to a particular material, due to a small red-shift caused by the dielectric surroundings, as illustrated in Figs 12 and 13. The characterization of plasmon resonances in metallic nanoparticles, as presented in Figs 11-13, has been done by finite element method of solution of Maxwell-Fresnel problem (utilizing COMSOL system) and by Mie approach [20].
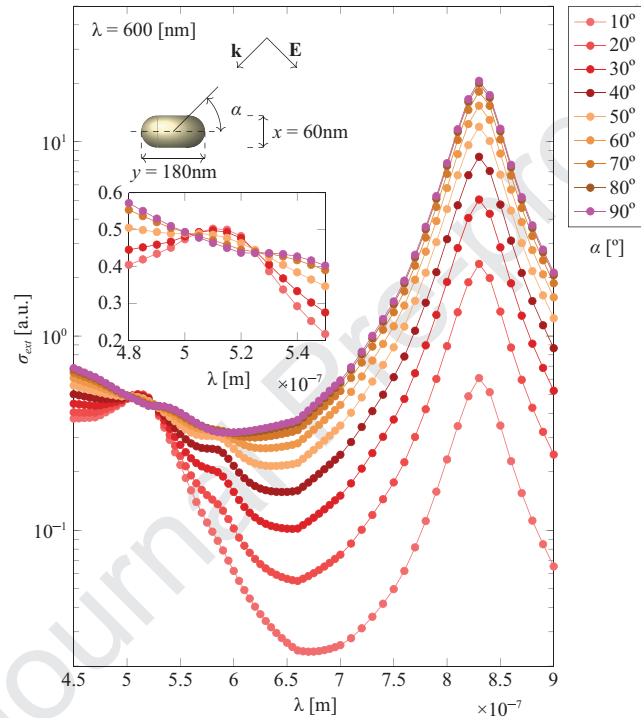

Figure 14: Dipole plasmon resonances in Au nanorod. Comparison of intensities of both mode of dipole plasmon (longitudinal and transverse ones). The relative intensity of both peaks changes with deviation of the incident e-m wave electric field polarization with respect to the nanorod orientation.
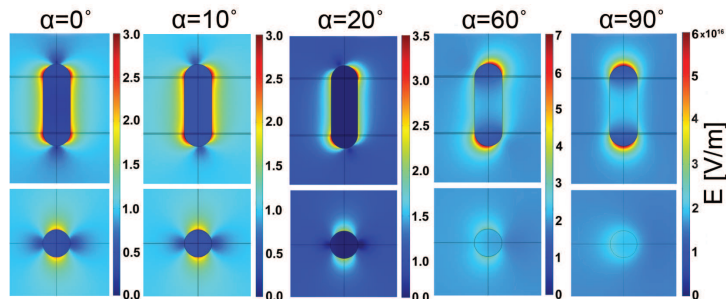

Figure 15: Changes in local field focusing around the Au nanorod with deviation of electric field of incident e-m wave from the direction of longer axis of the nanorod.
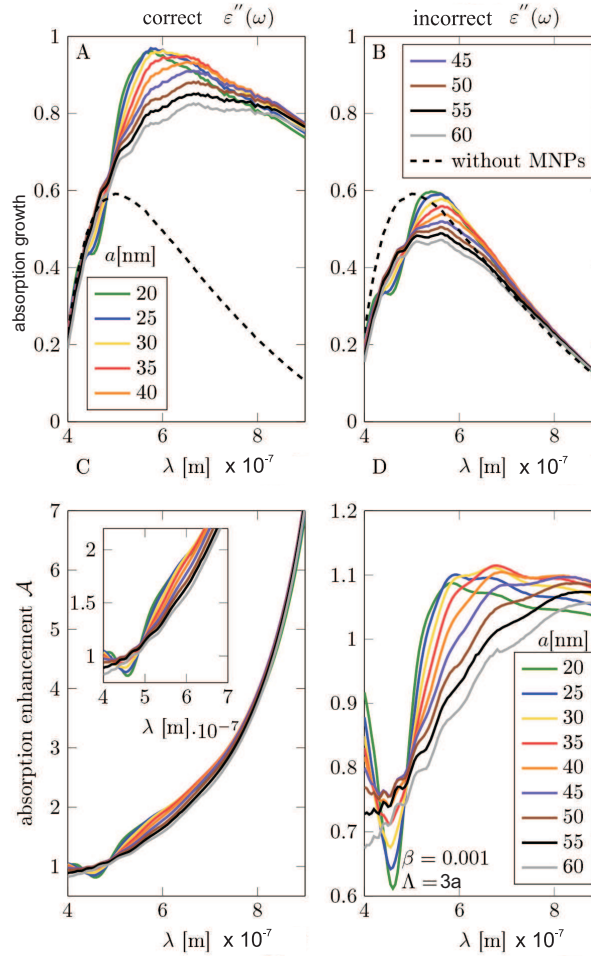
periodic model

Figure 16: The periodic model—(**A**,**B**): The absorption enhancement in the Si substrate as the function of the wavelength of incident electromagnetic wave for varying radius of metallic nanoparticles. (**C**,**D**): The efficiency rate growth as a function of the wavelength of incident electromagnetic wave for varying radius of nanoparticles. (**A**,**C**): The results obtained in the model using modified $\varepsilon''(\omega)$ (absorption of semiconductor and damping of plasmons) by the quantum corrections; (**B**,**D**): The results obtained in the model using non-modified dielectric functions taken from the measurement in bulk and in separation [45]. The calculation was made for MNP arrays with the period equal $\Lambda = 3a$ and the radius $a = 20, 25, 30, 35, 40, 45, 50, 55, 60$ nm.
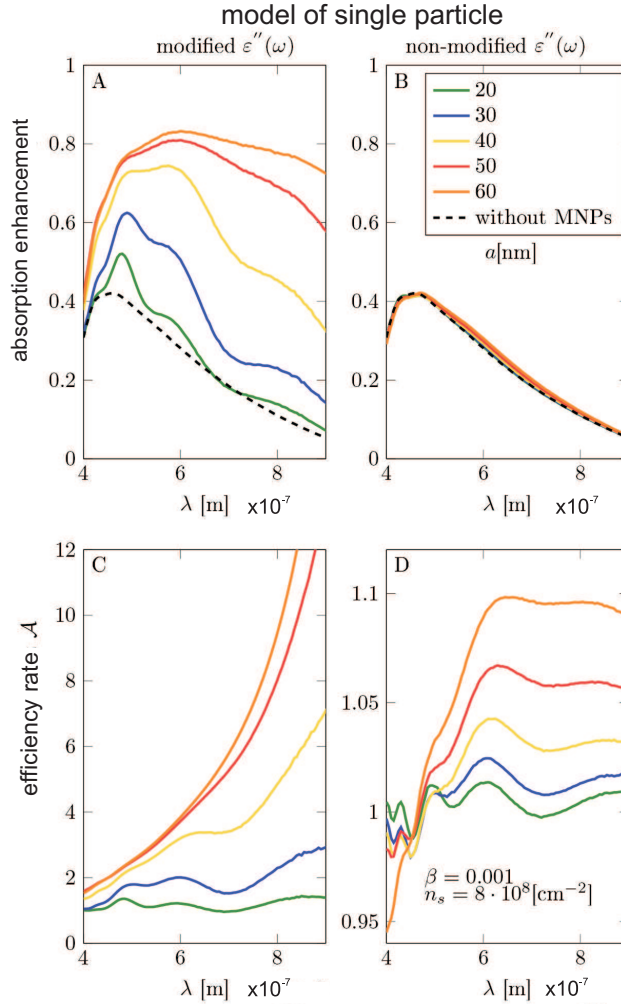
model of single particle

Figure 17: Single particle model—(**A**,**B**): The absorption growth in the Si substrate as a function of the wavelength of incident electromagnetic wave for varying radius of metallic nanoparticles (Λ— calculation cell size, accommodated to conserve surface density $n_s = 8 \times 10^8/\mathrm{cm}^2$). (**C**,**D**): The efficiency enhancement factor as a function of the wavelength of incident electromagnetic wave for varying size of nanoparticles and constant their concentration. (**A**,**C**): Results obtained in the model using modified $\varepsilon''(\omega)$ (absorption of semiconductor and damping of plasmons) by quantum corrections. (**B**,**D**): Results obtained in the model using non-modified dielectric function measured in bulk and in separation [45]. The calculations were made for on Si substrate deposited single MNP with radii $a = 20, 30, 40, 50, 60$ nm and for MNP effective (accommodated by Λ) concentration $n_s = 8 \times 10^8/\mathrm{cm}^2$.

C. Characterization of plasmon resonance in nanorod

Another method to better accommodate plasmon resonance in metallic nanoparticles to particular semiconductor substrate (with specific cut off by the forbidden energy) and to sun-light spectrum is the duplication of dipole plasmon resonance in nanorods or nanospheroids. Longitudinal and transverse plasmon oscillation energies differ in nanorods and may more precisely accommodate to the available part of the sun-light spectrum. In Fig. 14 we demonstrate the intensity of both plasmon resonance peaks in Au nanorod with respect to orientation of the electrical field of incident e-m wave versus the nanorod longer axis. We see that the domination of the longitudinal oscillations is quickly reduced when the electric field polarization deviates from the longer axis direction of the nanorod. As sun-light is not polarized and nanorods are distributed with random orientation, we can conclude that the privilege of the longitudinal mode is unimportant and strongly reduced, which is convenient to utilize both modes, longitudinal and transverse, to optimize plasmonic effect, as has been experimentally demonstrated in [16].

The same may be addressed to local strengthening of the electric field close to the nanoparticle curvature. In Fig. 15 we present how changes this field focusing with the deviation of the incident e-m wave polarization with respect to nanorod orientation. Privileges of this field concentration are strongly reduced for unpolarized sun-light and for random alignment of nanorods. This agrees with the general overestimation of the role of the field focusing in plasmon photovoltaic effect. As we show in the next Appendix D, the focusing of the local electric field causes not more than 10% only of the plasmon mediated absorption in the substrate semiconductor.

Figs 14 and 15 have been found by numerical finite element modeling of field distribution upon the COMSOL system.

D. Comparison of absorption plasmon strengthening with and without quantum corrections

By the direct comparison of the absorption of incident e-m wave energy in substrate semiconductor (Si) via mediation of plasmons in metallic nanoparticle (Au) deposited on the top of semiconductor layer for two situations, (left) when quantum corrections have been taken into account via the Fermi golden rule and (right) when only focusing of the local field is accounted for. We see that the focusing effect does not exceed 10% of the full effect when quantum corrections are included. This dismisses the validity of COMSOL simulations of by plasmon strengthening of photon absorption if quantum corrections are not taken into account. In Fig. 16 (for periodic deposition of Au nanoparticles on Si substrate) and Fig. 17 (for single Au nanoparticle deposited on Si) both contributions are compared.

Figs 16 and 17 have been found by numerical finite element modeling of the plasmonic effect upon the COMSOL system with predefined the dielectric functions of metallic nanoparticles and substrate semiconductor without quantum corrections (right panels in Figs 16 and 17) and with quantum corrections determined by the Fermi golden rule (left panels). By dashed lines are indicated spectral curves for absorption in Si without metallic nanoparticles. For more detailed analysis of this effect, cf. [21].

References

[1] D. M. Schaadt, B. Feng, E. T. Yu, Enhanced semiconductor optical absorption via surface plasmon excitation in metal nanoparticles, Appl. Phys. Lett. 86 (2005) 063106.

[2] S. Lim, W. Mar, P. Matheu, D. Derkacs, E. Yu, Photocurrent spectroscopy of optical absorption enhancement in silicon photodiodes via scattering from surface plasmon polaritons in gold nanoparticles, Journal of Applied Physics 101 (2007) 104309.

[3] M. Jeng, Z. Chen, Y. Xiao, L. Chang, J. Ao, Y. Sun, E. Popko, W. Jacak, L. Chow, Improving Efficiency of Multicrystalline Silicon and CIGS Solar Cells by Incorporating Metal Nanoparticles, Materials 8 (2015) 6761 – 6771.

[4] P. Matheu, S. Lim, D. Derkacs, C. McPheeters, E. Yu, Metal and dielectric nanoparticle scattering for improved optical absorption in photovoltaic devices, Applied Physics Letters 93 (2008) 113108.

[5] M. Losurdo, M. M. Giangregorio, G. V. Bianco, A. Sacchetti, P. Capezzuto, G. Bruno, Enhanced absorption in Au nanoparticles/a-Si:H/c-Si heterojunction solar cells exploiting au surface plasmon resonance, Sol. Energy Mater. Sol. Cells 93 (2009) 1749.

[6] L. Luo, C. Xie, X. Wang, Y. Yu, C. Wu, H. Hu, K. Zhou, X. Zhang, J. Jie, Surface plasmon resonance enhanced highly efficient planar silicon solar cell, Nano Energy 9 (2014) 112–120.

[7] S. Pillai, K. Catchpole, T. Trupke, M. Green, Surface plasmon enhanced silicon solar cells, Journal of Applied Physics 101 (2007) 093105.

[8] H. R. Stuart, D. G. Hall, Island size effect in nanoparticles photodetectors, Appl. Phys. Lett. 73 (1998) 3815.

[9] S. Pillai, K. R. Catchpole, T. Trupke, G. Zhang, J. Zhao, M. A. Green, Enhanced emission from Si-based light-emitting diodes using surface plasmons, Appl. Phys. Lett. 88 (2006) 161102.

[10] W. Jacak, E. Popko, A. Henrykowski, E. Zielony, G. Luka, R. Pietruszka, B. Witkowski, L. Wachnicki, M. Godlewski, L.-B. Chang, M.-J. Jeng, On the size dependence and the spatial range for the plasmon effect in photovoltaic efficiency enhancement, Sol. Energy Mater. Sol. Cells 147 (2016) 1.

[11] M.-J. Jeng, C. Zih-Y, Y.-L. Xiao, L.-B. Chang, J. Ao, Y. Sun, E. Popko, W. Jacak, L. Chow, The efficiency enhancement of silicon and CIGS solar cells by the incorporation of metal nanoparticles, Materials 8 (2015) 6761.

[12] J. Jacak, W. Jacak, Plasmon-induced enhancement of efficiency of solar cells modified by metallic nano-particles: Material dependence, J. Appl. Phys. 124 (2018) 073107. Https://doi.org/10.1063/1.5040014.

[13] L. D. Landau, L. M. Lifshitz, Quantum mechanics. Nonrelativistic theory, Pergamon Press, 1965.

[14] W. Zhang, M. Saliba, S. Stranks, Y. Sun, X. Shi, U. Wiesner, H. Snaith, Enhancement of perovskite-based solar cells employing core-shell metal nanoparticles, Nano Lett. 13 (2013) 4505.

[15] K. Yao, H. Zhong, Z. Liu, M. Xiong, S. Leng, J. Zhang, Y. Xu, W. Wang, L. Zhou, H. Huang, A. Jen, Plasmonic metal nanoparticles with core-bishell structure for high-performance organic and perovskite solar cells, ACS Nano 13 (2019) 5397.

[16] R. Wu, B. Yang, C. Zhang, Y. Huang, Y. Cui, P. Liu, C. Zhou, Y. Hao, Y. Gao, J. Yang, Prominent efficiency enhancement in perovskite solar cells employing silica-coated gold nanorods, J. of Phys. Chem. C 120 (2016) 6996.

[17] W. Ho, C. Hu, C. Yeh, Y. Lee, External quantum efficiency and photovoltaic performance of silicon cells deposited with aluminum, indium, and silver nanoparticles, Japanese Journal of Applied Physics 55 (2016) 08RG03.

[18] T. Temple, G. Mahanama, H. Reehal, D. Bagnall, Influence of localized surface plasmon excitation in silver nanoparticles on the performance of silicon solar cells, Solar Energy Materials and Solar Cells 93 (2009) 1978 – 1985.

[19] C. Uhrenfeldt, T. Villesen, A. Têtu, B. Johansen, A. Nylandsted Larsen, Broadband photocurrent enhancement and light-trapping in thin film Si solar cells with periodic Al nanoparticle arrays on the front, Optics Express 23 (2015) A525.

[20] C. F. Bohren, D. R. Huffman, Absorption and Scattering of Light by Small Particles, Wiley, New York, 1983.

[21] K. Kluczyk, C. David, J. Jacak, W. Jacak, On modeling of plasmon-induced enhancement of the efficiency of solar cells modified by metallic nano-particles, Nanomaterials 9(1) (2018) 3. Doi: 10.3390/nano9010003.

[22] J. Jacak, J. Krasnyj, W. Jacak, R. Gonczarek, A. Chepok, L. Jacak, Surface and volume plasmons in metallic nanospheres in semiclassical RPA-type approach; near-field coupling of surface plasmons with semiconductor substrate, Phys. Rev. B 82 (2010) 035418.

[23] L. D. Landau, E. M. Lifshitz, Field Theory, Nauka, Moscow, 1973.

[24] J. D. Jackson, Classical Electrodynamics, John Willey and Sons Inc., New York, 1998.

[25] M. Westphalen, U. Kreibig, J. Rostalski, H. Lüth, D. Meissner, Metal cluster enhanced organic solar cells, Sol. Energy Mater. Sol. Cells 61 (2000) 97.

[26] H. R. Stuart, D. G. Hall, Enhanced dipole-dipole interaction between elementary radiators near a surface, Phys. Rev. Lett. 80 (1998) 5663.

[27] K. Okamoto, I. Niki, A. Shvartser, Y. Narukawa, T. Mukai, A. Scherer, Surface plasmon enhanced spontaneous emission rate of' InGaN/GaN QW probed by time-resolved photolumimnescence spectroscopy, Nat. Mater. 3 (2004) 601.

[28] C. Wen, K. Ishikawa, M. Kishima, K. Yamada, Effects of silver particles on the photovoltaic properties of dye-sensitized TiO_2 thin films, Sol. Cells 61 (2000) 339.

[29] P. S. Kiriejew, Physics of Semiconductors, PWN, Warsaw, 1969.

[30] Y. Shao, Z. Xiao, C. Bi, Y. Yuan, J. Huang, Origin and elimination of photocurrent hysteresis by fullerene passivation in $ch_3nh_3pbi_3$ planar heterojunction solar cells, Nat. Commun. 5 (2014) 5784.

[31] C. Wu, K. Wang, X. Feng, Y. Jiang, D. Yang, Y. Hou, Y. Yan, S. Sanghadasa, S. Priya, Ultrahigh durability perovskite solar cells, Nano Lett. 19 (2019) 1251. Doi: 10.1021/acs.nanolett.8b04778.

[32] A. Kojima, K. Teshima, Y. S. T. Miyasaka, Organometal halide perovskites as visible-light sensitizers for photovoltaic cells, J. Am. Chem. Soc. 131 (2009) 6050.

[33] H. Kim, C. Lee, J. Im, K. Lee, T. Moehl, A. Marchioro, S. Moon, R. Humphry-Baker, J. Yum, J. Moser, Lead iodide perovskite sensitized all-solid-state submicron thin film mesoscopic solar cell with efficiency exceeding 9%, Sci. Rep. 2 (2012) 591.

[34] R. Wu, B. Yang, J. Xiong, C. Cao, Y. Huang, F. Wun, J. Sun, C. Zhou, H. Huang, J. Yang, Dependence of device performance on the thickness of compact tio_2 layer in perovskite/tio_2 planar heterojunction, J. Renewable Sustainable Energy 7 (2015) 043105.

[35] P. Docampo, J. M. Ball, M. Darwich, G. E. Eperon, M. J. Snaith, Efficient organometal trihalide perovskite planar-heterojunction solar cells on flexible polymer substrates, Nat. Commun. 4 (2013) 2761.

[36] W. S. Yang, J. H. Noh, N. J. Jeon, Y. C. Kim, S. Ryu, J. Seo, S. Seok, High-prformance photovoltaic perovskite layers fabricated through intramolecular exchange, Science 348 (2015) 1234.

[37] J. Xiong, B. Yang, R. Wu, C. Cao, Y. Huang, C. Liu, Z. Hu, H. Huang, Y. Gao, J. Yang, Efficient and nonhysteresis perovskite solar cells based on the simplest structure and without additives, Org. Electron. 24 (2015) 106.

[38] NREL, Nrel efficiency chart (2019). Https://www.nrel.gov/pv/assets/pdfs/best-research-cell-efficiencies.20190802.pdf.

[39] Z. Xiao, C. Bi, Y. Shao, Q. Dong, Q. Wang, Y. Yuan, C. Wang, Y. Gao, J. Huang, High yield perovskite photovoltaic devices grown by interdiffusion of solution-processed precursor stacking layers, Energy Environ. Sci. 7 (2014) 2619.

[40] R. Wu, J. Yang, J. Xiong, P. Liu, C. Zhou, H. Huang, Y. Gao, B. Yang, Eficient electron-blocking layer-free planar heterojunction perovskite solar cells with a high open-circuit voltage, Org. Electron. 26 (2015) 265.

[41] K. Zhang, Z. Wang, G. Wang, J. Wang, Y. Li, W. Qian, S. Zheng, X. S, S. Yang, A prenucleation strategy for ambient fabrication of perovskite solar cells with high device performance uniformity, Nature Communication 11 (2020) 1006.

[42] J. Liang, X. Han, J. Yang, B. Zhang, Q. Fang, J. Zhang, Q. Ai, M. Ogle, T.Terlier, A. Martí, J. Lou, Defect-engineering-enabled high-efficiency all-inorganic perovskite solar cells, Advanced Materials 31 (2019).

[43] J. Xu, C. Boyd, Z. Yu, A. Palmstrom, D. Witter, B. Larson, R. France, J. Werner1, S. Harvey, E. Wolf, W. Weigand, S. Manzoor, M. Hest, J. Berry, J. Luther, Z. Holman, M. McGehee1, Triple-halide wide–band gap perovskites with suppressed phase segregation for efficient tandems, Science 367 (2020) 1097.

[44] S. Feldmann, S. Macpherson, S. Senanayak, M. Abdi-Jalebi, J. Rivett, G. Nan, G. Tainter, T. Doherty, K. Frohna, E. Ringe, R. Friend, H. Sirringhaus, M. Saliba, D. Beljonne, S. Stranks, F. Deschler, Photodoping through local charge carrier accumulation in alloyed hybrid perovskites for highly efficient luminescence, Nature Photonics 14 (2020) 123.

[45] D. Aspnes, A. Studna, Dielectric functions and optical parameters of Si, Ge, GaP, GaAs, GaSb, InP, InAs, and InSb from 1.5 to 6.0 eV., Physical Review B 27 (1982) 985 – 1009.

The authors declare that there is no conflict of interest.

On behalf of all authors

J. E. Jacak